Measurements of the deuteron and proton magnetic form factors at large momentum transfers

P. E. Bosted, A. T. Katramatou, R. G. Arnold, D. Benton,* L. Clogher, G. DeChambrier, J. Lambert,† A. Lung, G. G. Petratos,‡ A. Rahbar, S. E. Rock, and Z. M. Szalata
The American University, Washington, DC 20016

B. Debebe, M. Frodyma, R. S. Hicks, A. Hotta,§ and G. A. Peterson
University of Massachusetts, Amherst, Massachusetts 01003

R. A. Gearhart
Stanford Linear Accelerator Center, Stanford University, Stanford, California 94309

J. Alster and J. Lichtenstadt
Tel Aviv University, Tel Aviv, Israel 69978

F. Dietrich and K. van Bibber
Lawrence Livermore National Laboratory, Livermore, California 94550
(Received 14 December 1989)

Measurements of the deuteron elastic magnetic structure function $B(Q^2)$ are reported at squared four-momentum transfer values $1.20 \leq Q^2 \leq 2.77$ $(\mathrm{GeV}/c)^2$. Also reported are values for the proton magnetic form factor $G_{Mp}(Q^2)$ at 11 Q^2 values between 0.49 and 1.75 $(\mathrm{GeV}/c)^2$. The data were obtained using an electron beam of 0.5 to 1.3 GeV. Electrons backscattered near 180° were detected in coincidence with deuterons or protons recoiling near 0° in a large solid-angle double-arm spectrometer system. The data for $B(Q^2)$ are found to decrease rapidly from $Q^2=1.2$ to 2 $(\mathrm{GeV}/c)^2$, and then rise to a secondary maximum around $Q^2=2.5$ $(\mathrm{GeV}/c)^2$. Reasonable agreement is found with several different models, including those in the relativistic impulse approximation, nonrelativistic calculations that include meson-exchange currents, isobar configurations, and six-quark configurations, and one calculation based on the Skyrme model. All calculations are very sensitive to the choice of deuteron wave function and nucleon form factor parametrization. The data for $G_{Mp}(Q^2)$ are in good agreement with the empirical dipole fit.

I. INTRODUCTION

Electron-deuteron scattering has long been the subject of intense theoretical and experimental studies. Elastic scattering in particular offers unique opportunities to study the electromagnetic form factors of the deuteron for the information they contain on the short-range nucleon-nucleon interaction and the influence of non-nucleonic degrees of freedom.

Elastic scattering at 180° probes the magnetization current distribution of the deuteron and directly measures the magnetic form factor. Theoretical calculations show that at large four-momentum transfer Q^2 this form factor is sensitive to the short-range nucleon-nucleon interaction, as reflected in the high-momentum components of the deuteron wave function. In the nonrelativistic impulse approximation (NRIA) the electron is pictured as interacting with one of the two constituent nucleons in the deuteron. Deviations from the NRIA can be due to isoscalar meson-exchange currents (MEC's), isobar configurations (IC's), relativistic corrections, six-quark ($6q$) configurations, or other quark effects. There are many approaches to calculating the deuteron elastic form factors. Relativistic calculations have been done both using light-front dynamics and in the instant frame solving the Bethe-Salpeter equation. These calculations generally have not included two-body currents. Many nonrelativistic calculations, including several in the Skyrme model, have investigated the influence of MEC's and isobar admixtures. Several approaches to nonrelativistic calculations that include hybrid admixtures of $6q$ configurations have led to substantially divergent results. Finally, asymptotic formulas based on dimensional counting and perturbative quantum chromodynamics (PQCD) have been used to predict the high-Q^2 shape of the magnetic structure function. To provide constraints on these models and to improve our fundamental understanding of the strong nuclear force, we made measurements of the magnetic form factor at Q^2 values extending from 1.20 to 2.77 $(\mathrm{GeV}/c)^2$. This more than doubles the kinematic range of previously available data, and covers the region where most, but not all, models predict a diffraction minimum and a secondary maximum.

Measurements of the proton magnetic form factor were made in the region $0.49 \leq Q^2 \leq 1.75$ $(\mathrm{GeV}/c)^2$, primarily for calibrations and efficiency measurements. Data were also taken over the quasielastic peak at incident electron energies $E=0.843$, 1.020, 1.189, and 1.281 GeV, as previously reported in a Letter.[1]

A. Kinematics and cross sections

Figure 1 shows the Feynman diagram for elastic electron scattering in the one-photon exchange approximation. Also shown are the relevant four-momenta in the laboratory system. For a given incident electron energy E, scattering angle θ, and scattered electron energy E', the four-momentum transfer squared Q^2 is defined as

$$Q^2=-q^2=4EE'\sin^2\tfrac{1}{2}\theta\ , \tag{1}$$

neglecting the rest mass of the electron and adopting $\hbar=c=1$. The invariant hadronic final state mass squared W^2 is

$$W^2=M^2+2M\nu-Q^2\ , \tag{2}$$

where $\nu=E-E'$ is the energy transfer from the electron, and M the mass of the target nucleus. For elastic scattering, $W^2=M^2$; and the scattered electron energy is given by

$$E'=\frac{E}{1+\frac{2E}{M}\sin^2\tfrac{1}{2}\theta}\ . \tag{3}$$

In the one-photon exchange approximation the cross section for elastic scattering of unpolarized electrons on unpolarized deuterons is given by

$$\frac{d\sigma}{d\Omega}=\sigma_M[A(Q^2)+B(Q^2)\tan^2\tfrac{1}{2}\theta]\ , \tag{4}$$

where

$$\sigma_M=\frac{\alpha^2E'\cos^2\tfrac{1}{2}\theta}{4E^3\sin^4\tfrac{1}{2}\theta} \tag{5}$$

is the Mott cross section for scattering from a structureless target including the recoil factor E'/E. The fine structure constant $\alpha=e^2/4\pi=\frac{1}{137}$. The elastic electric and magnetic structure functions $A(Q^2)$ and $B(Q^2)$ are given in terms of the charge, quadrupole, and magnetic deuteron form factors $G_C(Q^2)$, $G_Q(Q^2)$, and $G_M(Q^2)$ by

$$A(Q^2)=G_C^2(Q^2)+\tfrac{8}{9}\eta^2G_Q^2(Q^2)+\tfrac{2}{3}\eta G_M^2(Q^2) \tag{6}$$

and

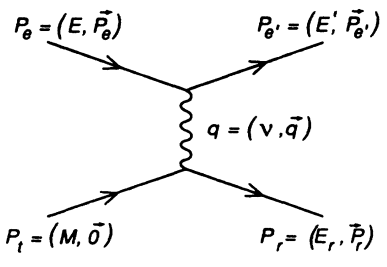

FIG. 1. Feynman diagram of elastic *e-d* or *e-p* scattering in the one-photon exchange approximation. Also shown are the relevant four-momenta in the laboratory system.

$$B(Q^2)=\tfrac{4}{3}\eta(1+\eta)G_M^2(Q^2)\ , \tag{7}$$

where $\eta=Q^2/4M_d^2$ and M_d is the deuteron mass. From these formulas it can be seen that electron scattering at $\theta=180°$ directly measures the magnetic structure function $B(Q^2)$ and hence the magnetic form factor $G_M^2(Q^2)$.

In the case of elastic electron-proton scattering, the cross section is given in terms of the proton electric and magnetic form factors $G_{Ep}(Q^2)$ and $G_{Mp}(Q^2)$ by

$$\frac{d\sigma}{d\Omega}=\sigma_M\left[\frac{G_{Ep}^2(Q^2)+\tau G_{Mp}^2(Q^2)}{1+\tau}+2\tau G_{Mp}^2(Q^2)\tan^2\tfrac{1}{2}\theta\right]\ , \tag{8}$$

where $\tau=Q^2/4M_p$ and M_p is the proton mass. It can be seen that elastic electron scattering at 180° directly measures $G_{Mp}(Q^2)$.

B. This experiment

The primary goal of this experiment was to measure the magnetic structure function $B(Q^2)$ of the deuteron up to the largest possible Q^2. The forward angle structure function $A(Q^2)$ (a combination of the charge, quadrupole, and magnetic form factors) has previously[2] been measured up to $Q^2=4$ (GeV/c)^2 and shows a smooth decrease from 10^{-4} at $Q^2=1$ (GeV/c)^2 to 10^{-7} at $Q^2=4$ (GeV/c)^2. Prior to this experiment, the data[3,4] for $B(Q^2)$ only extended slightly beyond 1 (GeV/c)^2. The predictions of most calculations and extrapolation of the previous data showed $B(Q^2)$ to be less than 1% of $A(Q^2)$ at large Q^2. These small values for $B(Q^2)$ dictated that the electron scattering angles should be close (within several degrees) to 180° so that the contributions from $A(Q^2)$ would not dominate. Since the cross section falls rapidly with Q^2, a large solid-angle 180° electron spectrometer and the thickest possible targets were needed to maintain reasonable counting rates. The use of long targets resulted in relatively poor resolution (0.3–0.5 %) due to the energy losses of the incident and back-scattered electrons in the target. This poor resolution was inadequate to distinguish elastically scattered electrons from electrons inelastically scattered from either the deuterium or the target aluminum endcaps. This problem dictated the use of a spectrometer centered at 0° to detect recoil deuterons in coincidence with back-scattered electrons.

This experiment, referred to as NE4, was carried out at the Stanford Linear Accelerator Center (SLAC) using electrons produced by the Nuclear Physics Injector and transported into End Station A (ESA). Data were taken in two running periods: one in May–July 1985 (NE4-I) and one in April–June 1986 (NE4-II). The electron spectrometer was taken apart and reassembled between NE4-I and NE4-II to allow for the running of another experiment.

A Monte Carlo computer program[5] was written to simulate the entire spectrometer system. The program traced particles from the targets to the detectors using detailed field maps that were made for each magnet. The effects of ionization loss, multiple scattering, finite target

length, detector resolutions, limiting apertures, and radiation by electrons were taken into account. It was used in the design of the experiment, during the data taking, and for data analysis.

The data for $B(Q^2)$ have been previously briefly reported[6] in a Letter. This paper provides additional details on the analysis procedures used and contains a more complete comparison of the data with available calculations. It is based on the Ph.D. thesis of Katramatou.[7] Many of the details on the constructure and calibration of the spectrometer system have been previously reported[8] and will not be repeated here. Additional details on the spectrometer as well as the analysis of the proton data can be found in the Ph.D. thesis of Petratos.[9]

This paper is organized as follows: The beam, targets, spectrometers, electronics, and all other equipment are described in Sec. II. The analysis methods and corrections to the data are discussed in Sec. III. The extraction of final electron-proton (*e-p*) and electron-deuteron (*e-d*) elastic cross sections and the results for $G_{Mp}(Q^2)$ and $B(Q^2)$ are given in Sec. IV. In Sec. V a summary of the existing calculations of $B(Q^2)$ is given and comparisons are made with the results of this experiment.

II. EXPERIMENTAL APPARATUS

Figure 2 shows a schematic diagram of the entire NE4 spectrometer system. The electron beam, after exiting the switchyard, was transmitted through the chicane of bending magnets $B1$,$B2$,$B3$ and the quadrupole triplet $Q1$,$Q2$,$Q3$ to the liquid deuterium and hydrogen targets. The back-scattered electrons were focused in the same triplet and transported through the bending magnets $B3$ and $B4$ to a detection system. The quadrupole triplet $Q1$,$Q2$,$Q3$ the bending magnets $B3$,$B4$, and the detector package constitute the electron spectrometer of the 180° system.

Downstream from the target, the incident electrons and the recoil deuterons or protons were focused through the quadrupole triplet $Q4$,$Q5$,$Q6$. They then passed through bending magnet $B5$, which deflected the electron beam in one direction towards a remotely movable water-cooled beam dump, and deflected the recoil nuclei in the other direction to be transported through magnets $B6$, $B7$, and $B8$ to a set of detectors. The quadrupole triplet $Q4$,$Q5$,$Q6$, the bending magnets $B5$,$B6$,$B7$,$B8$, and the detectors constitute the recoil spectrometer. The entire beam transport system up to the detectors was under vacuum and heavily shielded on all sides.

Signals from the detectors of the two spectrometers were sent to Counting House A to be processed by fast electronics. A VAX 11/780 computer was used to record on magnetic tape all relevant information about each event as well as general information about equipment used in the experiment. The same computer provided on-line analysis of a sample of the events throughout the experiment and was used for the final analysis.

The rest of this section provides a detailed discussion of the beam, targets, spectrometers, and detector packages and concludes with a description of the electronics and data acquisition system.

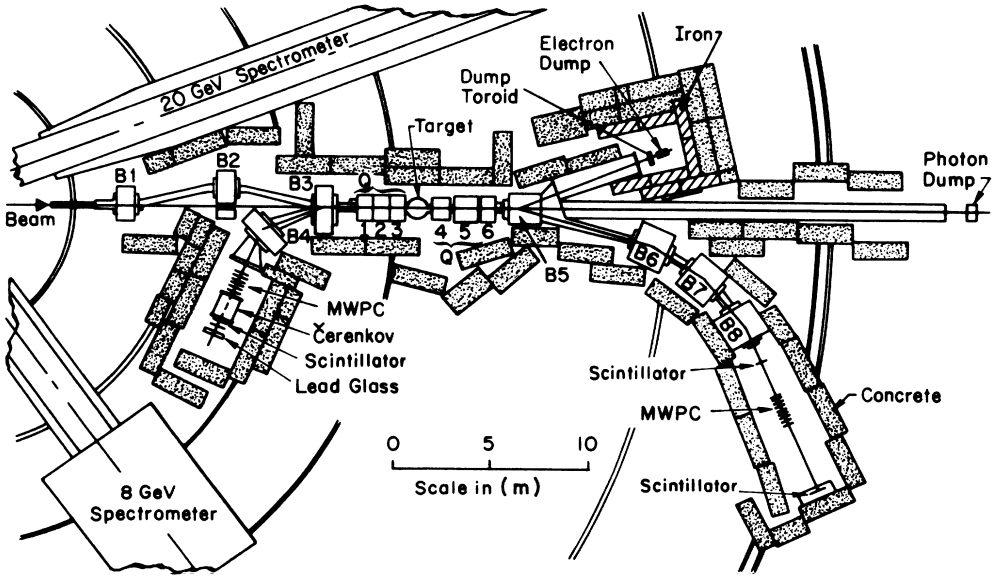

FIG. 2. A schematic diagram of the double-arm spectrometer system. The elements $B1$–$B8$ are dipole bending magnets and $Q1$–$Q6$ are quadrupoles. Also shown are the detector packages for the two spectrometers and the extensive shielding. This spectrometer system is described in detail in Ref. 8.

A. Beam

The electron beam was produced by the Nuclear Physics Injector[10] (NPI) located at Sector 25 of the Stanford Linear Accelerator. The beam was accelerated in the last six sectors to energies of 0.5–1.3 GeV. The peak current was as high as 50 mA in typically 1.6-μs-long pulses produced at a maximum repetition rate of 180 Hz. The beam energy setting was known[11,12] to an accuracy of $\pm 0.1\%$. The energy spread was typically limited to $\pm 0.5\%$ by high-power slits.

Because of the complexity of the spectrometer system, extra care was taken to keep the beam centered on the target. This was accomplished using two planes of wires located approximately 1 m upstream of the target. Each plane consisted of 25 CuBe wires 0.1 mm in diameter spaced 1.0 mm apart. The beam-induced secondary emission signals from the wires were digitized and read by an LSI-11 computer, which controlled steering magnets to keep the beam centered on the target. The beam spot size at the target was typically 1.0 cm in the horizontal by 0.5 cm in the vertical direction. The beam position at other points in the spectrometer system was periodically adjusted using five ZnS screens that could be inserted into the beam between data runs.

The charge in each incident beam pulse was measured by two identical toroidal charge monitor systems.[13] Each toroid was equipped with a calibration unit which simulated the electron beam by sending a precisely known charge through a single additional turn of wire passing through the toroid. The calibration and zero drift of the two toroids were systematically checked during the experiment. The measurements of the integrated beam charge by the two toroid systems were found to agree to within $\pm 0.3\%$. For each toroid, two independent sets of electronics were used to measure the charge, yielding results which agreed to within $\pm 0.2\%$ for a given toroid.

B. Targets

The target assembly consisted of three layers of target cells (see Fig. 3). The top layer contained liquid hydrogen, the second liquid deuterium, and the third was empty (the so-called "dummy" targets). Each of the layers could be oriented to provide four targets with nominal lengths of 40, 20, 10, and 5 cm, as can be seen in Fig. 4, which shows a top view of one of the cells. The target assembly rotated about its vertical axis and moved vertically under computer control to bring a specific target into the beam. The entire assembly was suspended in a cylindrical scattering chamber maintained at a pressure of about 10^{-7} Torr. Windows separating the chamber vacuum from the beam line vacuum were made of 0.025-mm-thick aluminum foil.

Data from the empty cell were used to correct the data taken with the liquid cells for the contributions from the aluminum endcaps. The empty targets had the same geometry as the full targets but with thicker endcaps to minimize the running time needed and to match the radiation length of the liquid targets.

The deuterium and hydrogen liquids were pressurized to two atmospheres and were circulated through the tar-

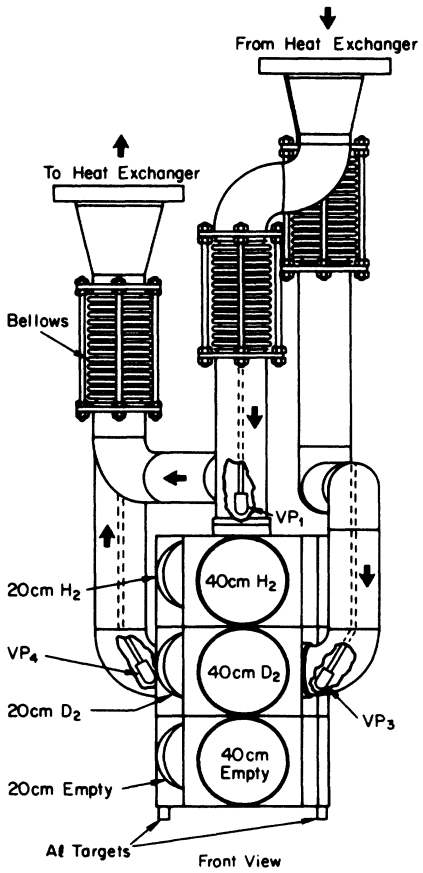

FIG. 3. Schematic front view of the liquid target assembly looking in the direction of the incident beam. Shown are the front endcaps of the 40-cm target orientation of the hydrogen, deuterium, and empty target cells. Also shown is the heat exchanger system, and the vapor pressure bulbs VP1–4 used for temperature measurements.

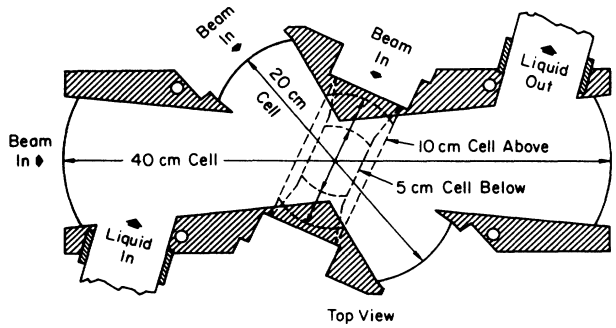

FIG. 4. Cross section of a top view of one of the target cells. The cell could rotate about its vertical axis under remote control to bring a specific target into the path of the beam. Also shown are the inlet and outlet for the target liquid.

gets cells using one 10-cm vane-axial fan for each liquid. They were circulated through heat exchangers in contact with liquid hydrogen at 21 K to absorb the deposited beam power. The temperature was measured at the inlet and at the outlet of each cell with vapor pressure thermometers. The average density of the liquid deuterium deduced from the temperature measurements was 0.170 ± 0.002 g/cm^3 and that of the hydrogen was 0.071 ± 0.001 g/cm^3. Measurements of scattered electron and recoil nuclei rates were made at different beam currents and repetition rates to check for possible local density changes due to beam heating along the beam direction. These measurements showed the density to be independent of beam current to better than 1%.

C. 180° spectrometer system

The main design requirements of the spectrometer system were the following.

(i) The electron spectrometer should have the largest possible solid angle for a variety of target lengths to maximize counting rates.

(ii) The solid angle of the recoil spectrometer should subtend that of the electron spectrometer for elastic kinematics so as to minimize solid angle corrections.

(iii) The momentum and angular resolutions of the electron and recoil spectrometers need only be moderate since elastic scattering events would be identified using double-arm coincidences.

Due to budget constraints, the spectrometer system was designed to utilize existing surplus magnets, chosen to maximize the solid angles and minimize the drift lengths. In the following paragraphs we give an overview of the system that was designed to meet these requirements. A more detailed description of the design and performance has been previously published.[8]

The electron arm and beam transport chicane are detailed in Fig. 5. As in other 180° systems, there were two overlapping channels: one for the incident beam and one for the back-scattered electrons. The beam traveled through the chicane of bending magnets $B1$,$B2$,$B3$ and along the magnetic axis of the quadrupole triplet $Q1$,$Q2$,$Q3$ to impinge on the target. Back-scattered electrons were focused by the same triplet and transported through the bending magnets $B3$ and $B4$ to a set of particle detectors. The quadrupole triplet provided the large gathering power for the relatively low-energy (0.2–0.6 GeV) back-scattered electrons while having little effect on the transported incident beam. Quadrupoles $Q1$ and $Q3$ focused in the vertical direction, while $Q2$ focused in the horizontal direction. For a thin target, the solid angle was 22.5 msr (±45 mrad horizontally by ±150 mrad vertically) averaged over a momentum acceptance range of ±4%. The momentum and scattering angle resolutions were typically ±0.4% and ±8 mrad, respectively.

The bend angle in $B3$ for back-scattered electrons was fixed at $\theta_{B3}=20°$. Since the ratio of incident to scattered electron momenta changed with kinematics, the deflection angle for incident electrons θ_{B1} varied in $B3$ (and hence in $B1$, which was run at the same current). For this reason, magnet $B2$, which had twice the deflection angle of $B1$ and $B3$, was placed on a movable cart permitting a range of deflection angles between 4° and 11.5°. The bend angle in $B4$ was fixed at 45°.

There were also two overlapping channels in the recoil arm, shown in detail in Fig. 6. Both the incident beam electrons and the recoil nuclei passed through the quadrupole triplet $Q4$,$Q5$,$Q6$ before entering the bending magnet $B5$, which bent the recoil nuclei and electrons in opposite directions. Recoil nuclei, with momenta from 0.7 to 2.3 GeV/c, were bent by 15° in $B5$, then by 17° in each of the magnets $B6$, $B7$, and $B8$. The ratio of electron to recoil nuclei momenta varied with kinematics, so that the

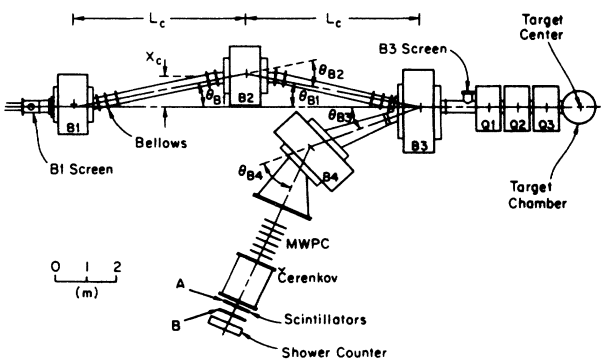

FIG. 5. The electron spectrometer and the beam transport system. Also shown are the vacuum system, the target scattering chamber, the electron detection system, and the $B1$ and $B3$ screens.

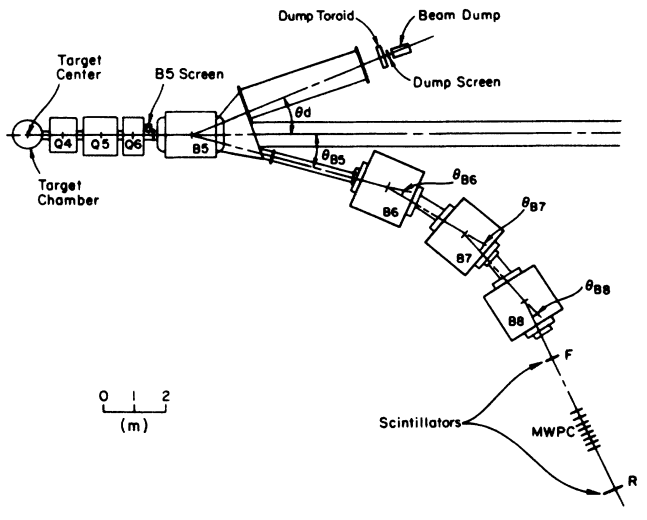

FIG. 6. The recoil spectrometer and the beam dump. Also shown are the vacuum system, the target scattering chamber, the recoil detection system, the dump toroid, and the $B5$ and dump screens.

deflection angle of the electrons ranged between 19° and 25°. For this reason, the beam dump was also placed on a movable cart.

Taking into account the angular and momentum spread resulting from multiple scattering and energy loss in the target, the focusing strengths of the quadrupole triplet $Q4,Q5,Q6$ were chosen to maximize the transmission of nuclei through the recoil spectrometer, while simultaneously achieving an acceptable beam spot size on the dump. As in the electron spectrometer, quadrupoles $Q4$ and $Q6$ focused vertically, while $Q5$ focused horizontally. For elastic *e-d* scattering, almost every deuteron associated with an electron detected in the electron spectrometer was transmitted to the recoil detectors. For a thin target, the solid angle of the recoil spectrometer was about 6 msr (±25 mrad horizontally by ±60 mrad vertically) averaged over a momentum acceptance of ±2%. The momentum resolution was typically ±0.3% and the resolution in the deuteron recoil angle was ±9 mrad.

The presence of bending magnets on the beam line and the dumping of the beam in ESA necessitated careful studies to meet the SLAC radiation safety and beam containment requirements and to reduce backgrounds in the detectors to acceptable levels. The spectrometer system was completely covered with a minimum thickness of 0.9 m of concrete, except in the target area. The dump was heavily shielded on all sides with a combination of iron and concrete, corresponding to an effective thickness of 3.7 m of concrete. A beam stopper was placed on the beam center line 15 m directly downstream of $B5$ to absorb the forward-peaked bremsstrahlung photons coming from the target and to stop the beam for a limited time in case magnet $B5$ lost power. Missteering in the chicane area was prevented using strategically located ion chambers and setting narrow tolerances on the currents in magnets $B1$, $B2$, $B3$, and $B5$.

D. Electron spectrometer detectors

The electron spectrometer detection system included six planes of multiwire proportional chambers (MWPC's) for track reconstruction, followed by a gas threshold Čerenkov counter, two planes of scintillation counters for trigger information and fast timing, and finally a total absorption shower counter for particle identification. Figure 7 shows the physical layout of the detectors.

The MWPC's (Ref. 14) were spaced 20 cm apart, and each had an active area of 35 cm by 93 cm. The chambers could be divided into two types depending on the orientation of their anode wires. The first type, called a "P" chamber, had 176 active anode wires 93 cm in length, parallel to the long axis of the chambers. A single support wire was placed perpendicular to the anode wires to prevent electrostatic instabilities. The second type had 480 active wires placed at $+30°$ or $-30°$ with respect to the short axis of the chambers (vertical direction), and were called "$+\theta$" or "$-\theta$" chambers, respectively. Adjacent wires of the θ chambers were electrically connected together effectively making 240 wires spaced 4 mm apart. The chambers were operated in a proportional mode using a gas mixture of 65.75% argon, 30.0% isobutane, 0.25% Freon 13B1, and 4% methylal. The typical operating voltage was 3600 V.

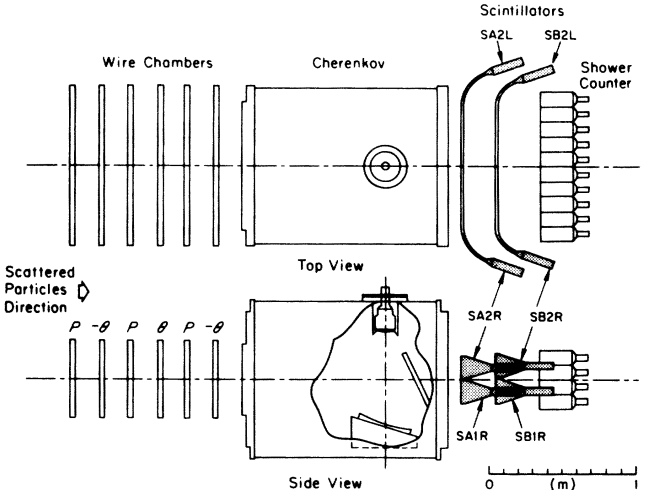

FIG. 7. The electron spectrometer detector arrangement. Particles entering from the left encountered six planes of wire chambers, a gas Čerenkov counter, two planes of scintillators, and a lead-glass shower counter.

The signals from the wires were amplified and delayed by 900 ns using electronics cards mounted on the chambers. The singles rates in each chamber ranged from 1 to 5 per pulse, resulting in a dead-time probability of 0.15–0.75 % per wire. An event trigger signal latched the signals, which were then read out serially by a dedicated CAMAC module. The tracking algorithm and performance of the chambers will be described in the next section.

The threshold Čerenkov counter consisted of a cylindrical aluminum tank 1.3 m long and 1.1 m in diameter. The entrance and exit windows were made of 0.041-cm-thick aluminum sheets with an area of 76.2 cm×40.0 cm. The Čerenkov light produced by high-velocity charged particles was first reflected by a rectangular flat-surfaced mirror to a concave spherical-surfaced mirror, which then focused it onto a 12.5-cm XP2041 Amperex photomultiplier tube (PMT). The combined reflectance of both mirrors was measured to be 90% over a wavelength range of 300–600 nm. The tank was filled with Freon-12 gas at atmospheric pressure which corresponds to a momentum threshold of 11.0 MeV/c for electrons and 3.0 GeV/c for pions. The efficiency for 0.2–0.6 GeV/c electrons as measured with a clean sample of electrons from *e-p* elastic scattering was found to be $>99.6\%$. Pions passing through the counter could only give a signal above discriminator level by producing knockon electrons or scintillation light. This happened for less than 1% of the pions. The singles rates in this counter ranged from 0.1 to a maximum of 2 per pulse.

The lead-glass shower counter, also used to separate electrons from pions and other backgrounds, consisted of 40 blocks arranged in a 4×10 array on an aluminum

base. The blocks were each 10×10 cm^2 in cross section and 25 cm long, and were made of DF6-type lead-glass manufactured by Nikon. This type of lead-glass has a density of 5.18 g/cm^3, a refractive index of 1.804, and a radiation length of 1.68 cm. Thus the shower counter was 14.88 radiation lengths, sufficient to contain over 98% of the longitudinal development of electron showers for momenta up to 0.6 GeV/c.

The blocks were wrapped with aluminized Mylar to separate the blocks optically and provide additional light collection capability. Each block was viewed by an R1911-05 Hamamatsu 7.5-cm PMT coupled to the block with a small amount of Dow Corning optical fluid, and operated at a typical voltage of 1500 V. Every lead-glass block was equipped with a fiber optics cable. The cables were joined together and illuminated in common by a light emitting diode. This was periodically used to check that the timing and operation of the PMT's were still working. The shower counter was found to have an energy resolution for electrons of about $12.5\%/\sqrt{E'}$ FWHM. These energy measurements will be discussed further in Sec. III. The singles rates for the sum of all blocks producing a signal above threshold ranged from 0.1 to 1 count per beam pulse.

The detector package also included two planes of plastic scintillators labeled A and B in Fig. 7. Both planes consisted of two scintillators ($A1$,$A2$ and $B1$,$B2$), 114.5 cm long by 17 cm high and 1.3 cm thick, each read out by two 5-cm 56AVP Amperex PMT's attached to the opposite ends. The A and B planes were part of the trigger and provided time-of-flight (TOF) information between the two spectrometer arms. Their efficiency was found to be greater than 98.8%. The singles rates for individual counters ranged from 0.1 to 1 per beam pulse.

E. Recoil spectrometer detectors

Figure 8 shows the detector package of the recoil spectrometer, consisting of two planes of plastic scintillation counters for TOF information and eight planes of MWPC's for tracking particle trajectories. The two arrays of plastic scintillators were spaced 7.0 m apart to provide recoil particle identification from the measured TOF between the two planes. TOF between the electron and recoil arm scintillators was also used to identify electron-recoil coincidences. The first scintillator array consisted of six counters ($F1-F6$) arranged in two rows of three each. Each counter was 15.2 cm wide by 14.0 cm high and 0.64 cm thick, and was read out by a 56AVP Amperex PMT run at typically 1800 V. The second array consisted of a single row of three counters ($R1-R3$) each 21.6 cm wide by 38.1 cm high and 0.95 cm thick and also connected to 56AVP Amperex PMT's. The singles rates for a typical counter ranged from 0.2 to 1 count per pulse.

The eight wire chambers of the recoil spectrometer were identical in construction to those of the electron spectrometer. Four P and four θ chambers were used, each spaced 20 cm apart. Only the central 176 wire pairs of the θ chambers were read out, resulting in an effective active area of 32 cm$\times$74 cm. The electronics and

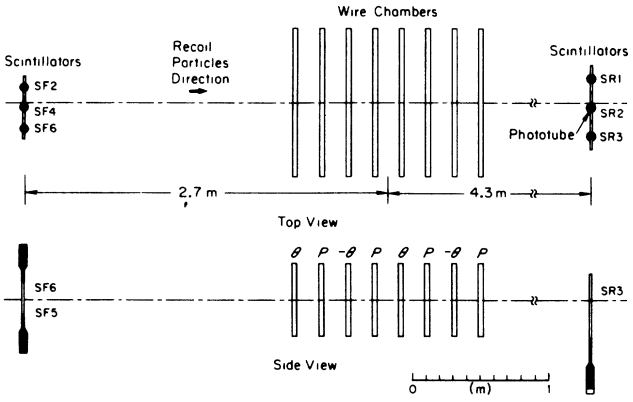

FIG. 8. The recoil spectrometer detector arrangement. Two planes of plastic scintillators were used for TOF information. Eight planes of wire chambers were used to measure particle tracks.

readout system for these chambers was the same as for the electron arm chambers. The singles rates for a given chamber ranged from 0.2 to 2 counts per pulse.

F. Electronics and trigger

The electronics setup for this experiment was relatively straightforward. The primary detector signals were PMT anode pulses coming from the total absorption shower counters, the Čerenkov counter, and the A and B scintillator planes (SA and SB). The 40 total absorption shower counter anode signals were first amplified by gain ten linear amplifiers and then split into two. One set of signals was sent to charge-integrating analog-to-digital converters (ADC's) and one set was linearly added to produce a single pulse (the shower sum signal). The pulse heights of the Čerenkov, shower sum, and the sum from the PMT's on either end of each scintillator were measured in ADC circuits. The analog signals also passed through discriminators to form logic signals for the shower counters, Čerenkov, and individual scintillators. These were counted in CAMAC scalers and timed relative to the trigger using time-to-digital converters (TDC's). The signals from both ends of each scintillator passed through mean timers. The mean-timer outputs were combined for each of the counters in a given plane to form logic signals for each plane (SA and SB).

The event-defining trigger was formed from a three-out-of-four coincidence of the Čerenkov, shower counter, SA, and SB logic signals. Additional triggers were infrequently generated at random in order to monitor the ADC pedestals. The width of the electron coincidence trigger was set to 25 ns. Two further coincidences were made with output widths of 40 and 65 ns to evaluate electronic dead-time corrections. Additional coincidences between various combinations of detectors were scaled to monitor accidental rates. An electronic filter was made to use only the first trigger in a given beam pulse to gate the ADC's, start the TDC's, latch the wire chamber signals, and send an interrupt to the computer. The correc-

tion for the loss in event rate was made by scaling the trigger coincidences both before and after the filter.

Signals from the recoil spectrometer were not used in the trigger. Pulse heights from each of the F and R scintillators were measured in ADC's, and discriminated to form logic pulses which were scaled and timed with TDC's. The individual logic signals from each plane were added to form SF and SR logic signals. A coincidence between these was also sent to a TDC to provide a hardware TOF signal. The gates for the recoil arm ADC's, the start signals for the TDC's, and the latch gate for the wire chambers all came from the trigger defined by the electron arm electronics, suitably delayed at each kinematic setting to account for the variation in TOF between back-scattered electrons and forward recoil particles.

G. Data acquisition

The primary purpose of the data acquisition computer was to record (on magnetic tape) the CAMAC information for each event trigger as well as information needed to deduce cross sections, such as accumulated toroid readings. The computer system included a small dedicated PDP-11/04 computer and a VAX 11/780. The PDP-11/04 computer read the event-related CAMAC electronics each time there was a trigger and transferred the data to shared memory in the VAX 11/780 for subsequent logging on magnetic tape.[15] In addition to event reading and logging, the VAX monitored the status of equipment used in the experiment, such as target position, magnet currents, detector high voltages, integrated toroid reading, beam energy and position, and the CAMAC hardware scalers. All this information was stored on the magnetic tape once every two or three minutes of data taking. It was therefore possible in the data analysis to discard small segments of data affected by problems such as a badly steered electron beam or a magnet current out of tolerance. Approximately 20% of data were rejected for such reasons.

III. ANALYSIS

This section details the analysis methods used to extract final cross sections from the raw data tapes. First, an electron was identified from a large background of pions using the Čerenkov and shower counters. The wire chambers were used to find the electron track and determine its momentum and scattering angle. Time-of-flight measurements between the front and rear scintillators in the recoil spectrometer identified recoil deuterons (or protons if e-p elastic cross sections were being measured). Time-of-flight between the electron and recoil arms was used to find electron-deuteron (or electron-proton) coincidences. The resulting missing momentum spectrum was corrected for the experimental inefficiencies. Two-parameter fits were then made to determine the percentage of counts due to elastic scattering and the percentage due to two-step background processes. The cross sections were deduced using the Monte Carlo generated acceptance values.

A. Identification of electrons

Electron identification and separation from pion background was achieved using the shower and Čerenkov counters. The requirement for the Čerenkov counter was simply that particles had to produce a signal above the discriminator threshold, which was set above the level of tube noise and below the average signal produced by two photoelectrons. Since the average number of photoelectrons produced was 15 for most of the experiment, the resulting efficiency was 99.7%. The efficiencies were measured using a pion-free sample of events from e-p elastic scattering. These events were required to have total absorption shower counter energies consistent with electrons, have a recoil proton in coincidence, and to have tracks that passed through the active area of the Čerenkov counter.

The shower energy deposited by a particle in the lead-glass counter was calculated by summing pedestal-subtracted pulse heights in blocks that had at least one of their edges within 5 cm of the track determined by the wire chambers. Each pulse height was multiplied by a correction coefficient to account for the variation in gain between the various blocks and to normalize the shower energy to that measured by the spectrometer. These coefficients were determined iteratively using a sample of electrons from e-p elastic scattering. Individual coefficients were found to have a momentum dependence of less than 3% over the momentum range of the experiment. The width of the normalized shower energy peaks for electrons was found to be $12.5\%/\sqrt{E'}$ FWHM, constant over the momentum range of the experiment

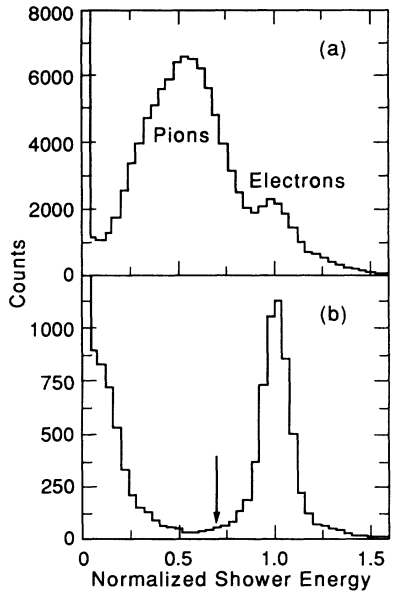

FIG. 9. Normalized shower pulse-height distributions: (a) for all events, and (b) for events with a Čerenkov counter signal above threshold. Data are for e-d scattering at $Q^2=1.49$ $(\mathrm{GeV}/c)^2$. The arrow indicates the cut used in identifying electrons.

(0.2–0.5 GeV/c). This resolution was close to that expected for the type of lead glass and PMT's used. The efficiency for electrons to produce a normalized shower energy greater than 0.7 was 98.5%, as determined from essentially pion-free samples of electrons from e-p elastic scattering. Most of the inefficiency was due to particles which traveled along the cracks between the blocks for long distances.

The ability of the shower and Čerenkov combination to reject pions and identify electrons is illustrated in Fig. 9. The top panel shows the normalized shower energy distribution for all triggers from an e-d elastic data run at $Q^2=1.48$ (GeV/c)^2. A broad peak is seen centered near 0.5 due to the pions, with a shoulder at 1.0 due to the electrons. The lower panel shows only the events for which there was also a signal in the Čerenkov. The pion peak has virtually disappeared, leaving a clean electron peak. A roughly exponential tail can be seen for particles with low shower energy. This is ascribed to random coincidences between room background particles firing both the Čerenkov and shower counters. This background was completely eliminated when a recoil deuteron was required to be in time coincidence with the electron.

B. Electron tracking

The tracking procedure began with the decoding of the digitized hit data from the wire chambers scanner words to identify the specific wires that fired in each chamber. Adjacent wires were treated as a single group. The position of the group was determined using the surveyed positions of the wire chambers and randomized over $\pm\frac{1}{2}$ wire spacing.

The track-finding algorithm consisted of two parts: The first part found tracks in the vertical direction using wire information of the P chambers only (P tracks). The second part found the horizontal components (x and θ) of the tracks using information from the θ chambers and the P tracks. At least four of the six wire chambers were required to have wires that had fired for the tracking algorithm to proceed. If so, the program searched for a track that fired at least two of the three P chambers and passed Monte Carlo determined cuts that ensured that the track pointed back to the target and forward through the shower counter. When there were three P chambers with hits forming the track, the hits were required to be collinear to within the uncertainties expected from multiple scattering and chamber alignments. If such a track was found, then tracks that had hits in only two P chambers were ignored.

For each P track the θ chambers were examined in a similar manner to find the track in the horizontal direction and determine the θ and x coordinate of the track at the center of the wire chamber system. Since the θ chambers have slanted wires, the P track information (ϕ and y) must first be known. At least two P and two θ chambers were required for a good track candidate. Tracks that could not have originated at the target or did not pass through the shower counter were rejected.

When the tracking algorithm found no tracks, a special search was done to test for tracks that passed close to the region of the support wires of the P chambers, where there were known inefficiencies. If three θ and one P chamber had fired, and the x coordinate was close to the support wire position of the other two P chambers, the track was kept.

When more than one track was found, the following purging criteria were applied:

(i) The normalized shower energy $S_{\rm trk}$ had to be greater than 0.6.

(ii) Tracks were required to have passed through the A and B scintillators that had fired.

(iii) Tracks were required to have reconstructed target production coordinates within the acceptance limits.

The performance of the electron arm wire chambers was studied with e-p elastic scattering. The efficiency of the wire chambers, $C_{\rm wce}$, was found to be independent of time and scattered electron momentum, with an average value of 98.5% for data with an average chamber counting rate of less than four hit wires per beam pulse. For runs with higher counting rates, the efficiency decreased noticeably due to the 450-ns dead time for each wire. For this reason, data runs or parts of data runs with average chamber counting rates greater than three per pulse were not used in the final data analysis. These high counting rates occurred when bad tuning of the linac caused substantial beam halos which scraped on various apertures in the spectrometer system. For runs with low singles rates, the average number of chambers per track was 5.8, and the individual chamber efficiencies were 97% on average.

Electron event candidates that passed all internal cuts of the track-finding program had their coordinates and momenta reconstructed at the center of the target. The reverse matrix elements that were used in the reconstruction were calculated with aid of the Monte Carlo program, and are given in Ref. 8.

C. Recoil particle identification

The recoil arm spectrometer was designed to detect protons or deuterons elastically recoiling from scattered electrons detected in the electron arm. Particles were identified in the recoil spectrometer by TOF between the F and R scintillator planes (F-R TOF). In the case of e-p elastic scattering, there was essentially no background in the identification of recoil protons. The main background for deuterons from e-d elastic scattering was a large flux (up to two per beam pulse) of protons coming from the reaction $\gamma d \rightarrow pn$ around 0 deg. The TOF difference between protons and deuterons over the 7-m separation between the scintillator planes ranged from 14.6 ns for $Q^2=1.20$ (GeV/c)^2 to 7.2 ns for $Q^2=2.77$ (GeV/c)^2, making the separation between the two signals relatively easy. After correcting for the track position and pulse-height variations, the F-R TOF resolution was 0.6 ns, producing a separation of 11 standard deviations between protons and deuterons at the highest Q^2 value of this experiment.

D. Recoil particle tracking

As for the electron side, the digitized information from the wire chambers was decoded to give the positions of

the wires or groups of wires for which there were signals. These were randomized over $\pm\frac{1}{2}$ wire spacing. The track-finding algorithm first found tracks in the vertical direction using the P chambers only, and then found the horizontal components (x and θ) using the θ chambers. Pairs of wires in different P chambers were chosen, and corresponding hypothetical tracks formed. The remaining P chambers were then tested to determine which had wires that fired within ± 3 wire spacings of where the track should pass. Straight line least-square fits were done to the coordinates of each P chamber track to find the ϕ and y coordinates at the center of the wire chamber system.

For each P track the θ chambers were examined in a similar manner to find the track in the horizontal direction and determine the θ and x coordinates of the track at the center of the wire chamber system. A minimum of three P and three θ chambers were required to form a track. If no track was found, the requirement was lowered to a total of five chambers with at least two chambers of each type.

Cuts were imposed to ensure that the track coordinates were within tolerances determined by the Monte Carlo calculation, and that they passed through the F and R scintillator planes. If more than one valid track was found, the best one was picked using F-R TOF, and reconstructed target position information.

The performance of the recoil arm wire chambers was studied with e-p elastic runs. The efficiency of the wire chambers C_{wcr} was found to be time independent and insensitive to the momentum of the recoil particle. The individual chamber efficiencies ranged from 82% to 98%. The poor efficiency of some of the chambers was not fully understood, but was most likely due to problems with the readout cards. The average number of hit chambers per track was 7.3, and the overall tracking efficiency was found to be $C_{\text{wcr}}=97.5\%$. No dependence on chamber singles rates was observed for the counting rates of this experiment.

As for the electrons, reverse matrix elements[8] determined from the Monte Carlo program were used to calculate the target coordinates and momenta from the track coordinates.

E. Double-arm events

Double-arm e-p and e-d events were separated from random background coincidences by TOF between the electron and recoil arm scintillators (el-rec TOF). The recoil time was defined as the average of the appropriate F and R times. The electron time was defined as the average of the times measured in the A and B counters intersected by the electron track. The timing resolution was optimized using calibration constants determined using essentially background-free e-p elastic scattering data. The final el-rec TOF values were corrected for the relative velocities of the individual recoil particles.

The average double-arm time resolution achieved was 0.6 ns. The clear identification of coincident deuterons is illustrated in Fig. 10, which shows scatter plots of F-R TOF vs el-rec TOF for the data at $Q^2=2.53$ (GeV/c)^2.

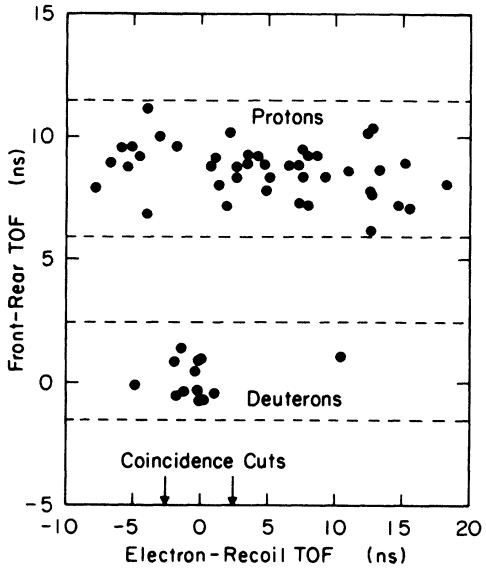

FIG. 10. TOF between the F and R scintillators in the recoil spectrometer vs double-arm TOF between the scintillators in the electron and recoil spectrometers. The data are at the e-d elastic kinematic setting of $Q^2=2.53$ (GeV/c)^2. The upper band corresponds to protons in random coincidence with electrons, while the lower cluster corresponds to deuterons coincident with electrons.

The upper band corresponds to random protons, which are cleanly separated from the cluster of deuterons. Also seen are two random deuterons that are not in time with the electrons. This background ranged from 3% to 10% of the coincident electrons, and was taken into account when extracting e-d elastic cross sections.

F. Electronics dead-time

The intrinsic dead time of the electronics caused a small loss of triggers. This loss was measured using trigger coincidence modules with larger output widths (40 and 65 ns) than the one used to trigger the computer, which had an output width of 25 ns. A straight line fit was made to the number of counts recorded for each of these three coincidences versus output width. The dead-time correction C_E was equal to the ratio of the intercept at 0 ns to the number of actual computer triggers. The values of C_E did not exceed 1.003 for the e-d elastic runs, and 1.033 for the e-p elastic runs. These values were in good agreement with calculations based on the counting rates in each detector and the known time response of the electronics modules.

G. Computer dead time

The CAMAC electronics and computer readout program were designed only to read out one event per beam pulse, so that a correction was needed for multiple events per beam burst. This correction was made using scalers that counted the number of triggers both before and after the module that limited the number of computer triggers to one per pulse. The ratio was applied as a multiplica-

tive factor to the number of recorded events in each data run. The value of this correction factor C_C did not exceed 1.06 for *e-d* runs, and was typically around 1.15 for *e-p* runs with a maximum value of 1.40. The error on this correction was negligible.

H. Recoil scintillator dead time

A flux of up to two protons per beam pulse caused dead time in the recoil side scintillator electronics. Any stray particle passing through a scintillator before the arrival of the recoil particle associated with a detected electron would stop the TDC early. Since both the *F* and *R* TDC's were required to be in the valid range to separate deuterons from protons, the correction could be substantial. The dead-time correction C_T for *e-d* elastic runs ranged from 1.01 to 1.05, depending on the proton rates per beam pulse. For *e-p* elastic runs C_T ranged from 1.01 to 1.06. During the second half of the data taking (NE4-II), gates were applied to the signals going to the *F* and *R* TDC's that reduced this correction by a factor of approximately 2 compared to the first half of the experiment.

I. Detector inefficiencies

The inefficiency of each detector was calculated from the number of times the specific detector had given no signal, but all the other ones had detected a double-arm event. Electron-proton double-arm elastic data were used. The total electron detector efficiency correction factor C_{es} was the inverse of the product of the efficiencies of the shower counter, the Čerenkov counter, the *A* and *B* scintillators, and the wire chambers. It was found to be independent of momentum and equal to 1.035 ± 0.007, for NE4-I, and 1.040 ± 0.007 for NE4-II. For the recoil detectors the total efficiency correction factor C_{rs} was the inverse of the product of the efficiencies of the *F* and *R* scintillators and the wire chambers. The *F* and *R* scintillator efficiencies for NE4-I were 96.5% and 99.1%, respectively, with the inefficiencies principally due to gaps between the individual scintillators. The efficiencies for NE4-II were increased to 99.8% and 99.2% for the *F* and *R* counters, respectively, by overlapping the counters slightly. The C_{rs} correction was independent of kinematics and equal to 1.072 ± 0.017 for NE4-I and 1.035 ± 0.010 for NE4-II.

J. Recoil nuclear interactions

A correction was applied for the loss of recoil particles that underwent elastic and inelastic nuclear collisions along their path through the target and detector materials. For the deuterium data, the corrections in the target were estimated from the proton-proton (*p-p*) and proton-neutron (*p-n*) total cross sections.[16] The deuteron-deuteron cross section was approximated as being twice the sum of the *p-n* and *p-p* total cross sections, and it was assumed that once a deuteron interacted in any way in the target it was lost. The correction factor depended on the target length and ranged from 1.033 ± 0.008 for the 10-cm target to 1.13 ± 0.03 for the 40-cm target. The target corrections to the *e-p* elastic data were calculated using the *p-p* total cross sections with the assumption that all protons interacting in the target were lost. The *e-p* corrections ranged from 1.005 ± 0.001 for the 5-cm target to 1.023 ± 0.006 for the 40-cm target.

To apply an approximate correction for the nuclear interactions of protons in the detector materials, it was assumed that half of the protons that suffered nuclear interactions were lost and not registered properly in the subsequent detectors. The percentage of protons lost in each material was approximated as $(T_m/2)/\lambda_T$, where T_m is the thickness of the material in g/cm^2 and λ_T is the collision length for nucleons in nuclear matter.[17] To account for the inherent uncertainty of this calculation, a 50% error was assigned to the calculated value. The correction was estimated to be 1.029 ± 0.015. For the deuterons the corrections were approximated as $(2T_m/2)/\lambda_T$, where the factor of 2 accounts for the two nucleons in the deuteron. The correction was estimated to be 1.058 ± 0.029. The total recoil nuclear interaction correction C_{NI} was the product of the corrections for losses in the target and detector materials.

K. Recoil spectrometer y'-offset corrections

The data analysis showed an offset relative to the Monte Carlo predictions for the y' (vertical position) distributions of particles at the recoil detectors. This offset is attributed to a relative misalignment of one or more of the recoil spectrometer quadrupoles with the beam axis, and caused some of the recoil particles to miss the detectors. The effect was simulated with the aid of the Monte Carlo program by introducing an offset of a few millimeters in the magnetic axis of the quadrupole triplet $Q4$–$Q6$. An offset in y'_0 at the target is translated to a y' offset through the $(y|y_0)$ matrix element. This matrix element is large (-5.6 cm/cm) for the recoil spectrometer. Figure 11 shows the relative decrease in the double-arm

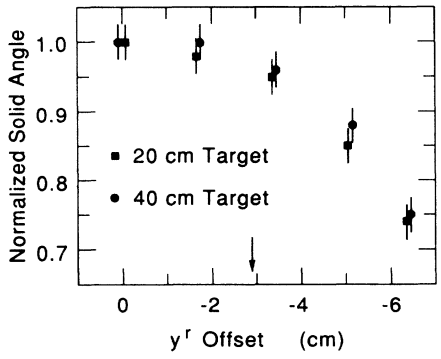

FIG. 11. Double-arm solid angle as a function of central recoil arm vertical position y', normalized to the value at $y'=0$. The arrow indicates the average y' offset for *e-d* elastic kinematic points. The solid squares are for the kinematic point at $Q^2=1.74$ (GeV/c)^2, while the solid circles are for $Q^2=2.48$ (GeV/c)^2.

effective solid angle for two of the kinematic settings of the experiment as a function of the y^r distribution centroid. The y^r distributions for *e-p* elastic scattering were narrow and the number of recoil protons lost was negligible. The distributions of recoil deuterons from *e-d* elastic scattering were significantly wider (due to differences in kinematics) and suffered ~5% losses. The offsets for the *e-d* elastic runs were determined from the distributions of the background protons from photoproduction processes. The average y^r was found to be -2.8 cm. No systematic trend with kinematics was observed. The effective double-arm solid angle was calculated from the Monte Carlo results taking into account the observed y^r offsets at each kinematic point.

L. Momentum calibration of the spectrometers

The central momentum of the electron spectrometer was known with an accuracy of $\pm 0.1\%$ in the momentum range of 230–350 MeV.[8] This calibration was made using elastic electron-proton runs and the known beam energy to study the deviations of the centroids of the x^e and θ^e elastic peaks from the nominal values ($x^e=0$, $\theta^e=0$). The same study estimated the central momentum uncertainty at the maximum spectrometer setting [540 MeV at $Q^2=2.77$ (GeV/c)^2] to be less than $\pm 0.25\%$. The momentum calibration was checked experimentally for each of the *e-d* runs using the pions photoproduced near 180° from the target. The end points of the experimental pion distributions were found to be consistent with that calculated from kinematics, as can be seen in Fig. 12. The arrows indicate the largest possible momentum for a pion produced from the upstream end of the target. Checks of the momentum calibration were also made using the observed position of the *e-d* elastic peaks at $Q^2=1.2$ and 1.5 (GeV/c)^2. Checks at higher Q^2 were not possible due to a combination of poor statistics and a two-step background that will be discussed below.

The recoil spectrometer was calibrated in the momentum range 1.5–2.5 GeV/c with an electron beam and in the range 0.7–1.5 GeV/c with double-arm *e-p* elastic scattering. For the high-momentum calibration, the polarity of magnets $B5$–$B8$ was reversed and a low-intensity electron beam was run through the spectrometer. The fields of these magnets were adjusted to center the beam on two fluorescent screens placed 3.8 m apart on the spectrometer axis after $B8$. For central momenta below 1.5 GeV/c the magnet currents were set to center the proton x^r and θ^r elastic peak distributions with respect to the spectrometer axis using the *e-p* double-arm runs. The two methods agreed in the region where they overlapped.

M. Monte Carlo comparisons

As illustrated in Ref. 8, Monte Carlo predictions and observed electron-proton elastic distributions were in very good agreement. Comparisons of the four electron side distributions x^e, θ^e, y^e, and ϕ^e showed almost perfect agreement. On the recoil side, the distributions for the x^r and θ^r, both of which roughly measure relative momentum, were slightly wider in the data than predicted by the Monte Carlo calculations. The widths of the y^r and ϕ^r distributions were in good agreement with the Monte Carlo predictions, but the centroids were shifted, as discussed above.

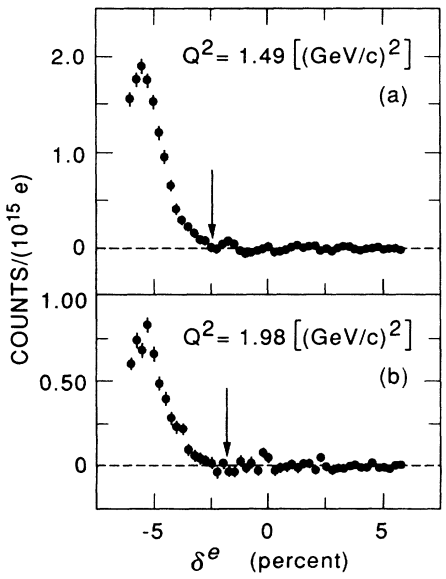

FIG. 12. Inclusive pion spectra (counts/10^5 electrons) in the electron spectrometer versus reconstructed relative momentum: (a) $Q^2=1.49$ (GeV/c)^2, and (b) $Q^2=1.98$ (GeV/c)^2. The arrows show the expected end points of the pion distribution from the upstream end of the target.

IV. EXPERIMENTAL CROSS SECTIONS AND $B(Q^2)$

A. Electron-proton elastic cross sections

Electron-proton elastic cross sections were measured for a range of incident electron energies from 0.504 to 1.286 GeV, corresponding to $Q^2=0.49$–1.75 (GeV/c)^2. The Monte Carlo program was used to calculate the effective single- and double-arm solid angles for each of these data points, including radiative corrections. The effective solid angles varied slowly with beam energy for a given target length because of differences in electron radiation losses. For a given beam energy they decreased linearly with target length due to both the loss in average geometrical acceptance and to the increased loss of electrons due to bremsstrahlung. For a typical beam energy of 1.02 GeV, the single-arm effective solid angle can be parametrized as $d\Omega(t)=19.5-0.16t$ msr, where t is the target length in centimeters. The corresponding double-arm acceptance is $18.5-0.17t$ msr.

The elastic electron-proton cross sections were calculated using

$$\frac{d\sigma}{d\Omega}=\frac{N_{ep}C_{\text{eff}}}{N_i TF(Q^2)d\Omega_{\text{MC}}(E,T)}\ , \tag{9}$$

where N_{ep} is the number of single-arm or double-arm elastic *e-p* events; N_i is the number of incident electrons; $C_{\text{eff}}=C_{\text{es}}C_{\text{rs}}C_C C_E C_T C_{\text{NI}}$ for double-arm and C_{eff}

$=C_{es}C_C C_E$ for single-arm cross sections, where C_{es} is the electron arm detector efficiency correction, C_{rs} is the recoil arm detector efficiency correction, C_C is the computer dead-time correction, C_E is the electronics dead-time correction, C_T is the recoil scintillator dead-time correction, and C_{NI} is the nuclear interaction correction; T is the target length in nuclei/cm^2; $d\Omega_{MC}(E,T)$ is the effective single- or double-arm solid angle from the Monte Carlo run under identical conditions as the measurements, including the acceptance-dependent part of the radiative corrections; and $F(Q^2)$ is the portion of the radiative corrections independent of the acceptance cutoff (see the discussion in Ref. 8).

Electron-proton elastic cross sections were measured at each beam energy with several of the four hydrogen targets available and were found to be independent (within errors) of the target length used, for both single-arm and double-arm cross sections. This shows that the Monte Carlo model correctly predicts the differences in effective solid angles due to radiation, multiple scattering, and ionization energy loss, and that the target length dependence of the nuclear interaction correction is correct.

A further test of the Monte Carlo model comes from comparing double-arm and single-arm cross sections. The ratios (averaged over target length) are shown in Fig. 13 and listed in Table I. The errors include only the portion of the statistical and systematic errors that do not cancel in the ratio, with the largest contributions coming from the uncertainties in the nuclear interaction corrections, the y^r offset correction, the F and R scintillator efficiencies and dead times, and differences in single-arm and double-arm radiative corrections. It can be seen that all the single-arm to double-arm cross section ratios are consistent with unity, indicating the Monte Carlo description of the differences in single- and double-arm acceptance is accurate.

The final single-arm cross sections, averaged over all target lengths used, are listed in Table I. The systematic errors are dominated by the following:

(i) the estimated uncertainty in the geometric solid angle of ±2% coming from the possible misalignment of geometric apertures, uncertainties in the location of the magnetic axes of the quadrupoles and their gradients, and uncertainties in the focusing strengths of $B3$ and $B4$ from the pole face rotations;

(ii) the estimated ±2% uncertainty in the evaluation of the radiative corrections with the Monte Carlo method; and

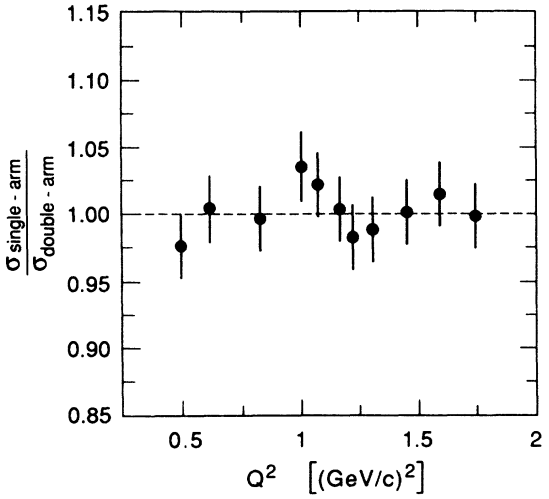

FIG. 13. Ratio of single-arm to double-arm *e-p* elastic cross sections as a function of Q^2. The results are averaged over the different target lengths used at each kinematic point. The errors are the systematic uncertainties that do not cancel in the ratio of the two cross sections.

TABLE I. Results for the 180° elastic electron-proton measurements. Given at each value of Q^2 are the ratio of single-arm to double-arm cross sections, the ratio of the single-arm cross section to that evaluated using the dipole form for $G_{Mp}(Q^2)$, and the experimental value for $G_{Mp}(Q^2)/G_D(Q^2)$ extracted from the single-arm cross section. All results have been averaged over all targets used at each value of Q^2. The errors on the ratio of single-arm to double-arm cross sections include only the portion of the systematic errors that do not cancel in the ratio.

Q^2 (GeV/c)^2	$\sigma_{single}/\sigma_{double}$ ±syst	$\sigma_{single}/\sigma_{dipole}$ ±stat±syst	$G_{Mp}(Q^2)/\mu_p G_D(Q^2)$ ±stat±syst
0.49	0.977±0.027	0.956±0.011±0.033	0.978±0.006±0.016
0.62	1.004±0.027	0.976±0.008±0.033	0.988±0.004±0.016
0.83	0.996±0.027	0.997±0.004±0.030	0.998±0.002±0.015
1.01	1.035±0.027	1.042±0.017±0.033	1.021±0.009±0.016
1.08	1.021±0.027	1.057±0.011±0.030	1.028±0.006±0.015
1.17	1.003±0.027	1.031±0.004±0.033	1.016±0.002±0.016
1.23	0.982±0.207	1.035±0.027±0.033	1.017±0.014±0.016
1.31	0.988±0.027	1.031±0.005±0.033	1.016±0.003±0.016
1.45	1.000±0.027	1.056±0.007±0.030	1.028±0.004±0.015
1.61	1.014±0.027	1.046±0.007±0.030	1.023±0.003±0.015
1.75	0.998±0.027	1.031±0.007±0.030	1.015±0.004±0.015

(iii) the uncertainty in the electron arm detector efficiencies.

The measured cross sections have been divided by those obtained using the dipole form for the proton form factors:

$$G_{Ep}(Q^2)=G_D(Q^2)=(1+Q^2/0.71)^{-2}\ , \tag{10}$$

$$G_{Mp}(Q^2)=\mu_p G_D(Q^2)\ , \tag{11}$$

where Q^2 is in $(\mathrm{GeV}/c)^2$ and $\mu_p=2.79$ is the magnetic moment of the proton. The systematic errors include the uncertainty in the evaluation of the dipole cross section due to the $\pm 0.1\%$ uncertainty in incident beam energy. Also listed in Table I are the extracted values of the proton magnetic form factor $G_{Mp}(Q^2)$ divided by the dipole form. The results for $G_{Mp}(Q^2)/\mu_p G_D(Q^2)$, displayed in Fig. 14, are a few percent lower than those of four previous experiments,[18–21] but are in good agreement with the results of a recent high-precision experiment.[12] It can also be seen that the results are in substantially better agreement with the dipole fit than with three commonly used parametrizations, shown as the dashed,[22] dotted,[23] and solid[24] curves. The first two parametrizations are fits to previous proton data using vector dominance models incorporating terms from the ρ, ϕ, and ω mesons. The last curve is constrained by vector dominance at low energies and PQCD at high energies, and comes from a fit to both previous proton and neutron data. New fits should be performed using the data from this experiment and from Ref. 12 to obtain a more accurate parametrization of the proton magnetic form factor.

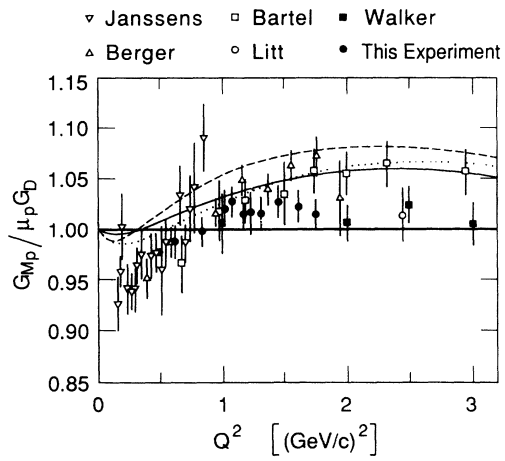

FIG. 14. Results for the proton magnetic form factor divided by the dipole fit from this experiment and from Janssens *et al.* (Ref. 21), Bartel *et al.* (Ref. 18), Walker *et al.* (Ref. 12), Berger *et al.* (Ref. 19), and Litt *et al.* (Ref. 20). The errors for the data points from this experiment include both total systematic and statistical errors added in quadrature. Also shown are parametrizations from Höhler *et al.* (Ref. 22, dashed), Iachello *et al.* (Ref. 23, dotted), and GK (Ref. 24, solid).

B. Electron-deuteron elastic cross sections

The elastic electron-deuteron cross sections were calculated using

$$\frac{d\sigma}{d\Omega}=\frac{N_{ed}C_{\mathrm{eff}}}{N_i TF(Q^2)d\Omega_{\mathrm{MC}}(E,T)}\ , \tag{12}$$

where N_{ed} is the number of double-arm elastic *e-d* events corrected for random *e-d* coincidences, and true *e-d* coincidences coming from multistep background reactions. The random background ranged from 1% to 13% of the number of *e-d* coincidences. The contributions from multistep background reactions will be discussed in the following subsection. Endcap contributions were found to be negligible. The rest of the symbols used in Eq. (12) have the same meaning as those used in Eq. (9).

C. Background separation for *e-d* elastic

Examinations of the final electron and deuteron momentum distributions showed an excess of double-arm counts with low momentum in both distributions, compared to the number expected from radiative processes. The excess was negligible at the two lowest Q^2 points, but was very significant at higher Q^2. We identified two different multistep reactions induced by bremsstrahlung photons in the target that can produce double-arm *e-d* coincidences in this kinematic region. The first possible reaction is $\gamma d\rightarrow\pi^0$ at 180°. The π^0 decays immediately into two photons, one of which can pair produce in the target material between the production point and quadrupole $Q3$ to give an electron with high enough energy to be detected. The second process is Compton scattering from the deuteron $\gamma d\rightarrow\gamma d$ at 180°. The scattered photon can pair produce as above to give an electron detected by the electron spectrometer. The probability for detecting an electron from $\gamma d\rightarrow\gamma d$ is larger than for $\gamma d\rightarrow\pi^0 d$ since the latter involves an extra decay. On the other hand, the Compton cross section is expected to be much smaller. In both reactions, the distributions of deuteron momenta approximately follow the bremsstrahlung shape, with a maximum momentum close to that for *e-d* elastic scattering. The electron momentum distribution from either reaction is also continuous, and decreases rapidly as a function of momentum up to a maximum momentum close to that for elastic scattering. The rate of decrease is more rapid for π^0 production than for Compton scattering due to the extra two-body decay step involved.

For both possible background reactions the electron and deuteron typically have less momentum than for elastic scattering, so a convenient variable to help in separating the two-step processes from elastic scattering is the missing momentum $\delta_{\mathrm{mm}}=\delta^e+\delta^r$, where δ^e and δ^r are the percentage momentum deviations from the elastic peak settings in the electron and recoil spectrometers, respectively. The distributions of *e-d* coincidences as a function of missing momentum are shown in Figs. 15 and 16. Clear elastic peaks can be seen near $\delta_{\mathrm{mm}}=0$ for the two lowest Q^2 points, with no counts in the kinematically forbidden positive momentum region, and a few counts at negative missing momentum consistent with radiative

processes. For the higher Q^2 points, again there are no counts at large positive δ_{mm}, which could occur if the spectrometer momentum calibrations were wrong, or there were counts coming from the aluminum target endcaps. The higher Q^2 points show a clear excess of counts at low δ_{mm}, with a shape consistent with expectations for the two-step backgrounds discussed above. The complete lack of counts above $\delta_{mm}=2\%$ supports the assumption that the excess counts at low δ_{mm} come from the deuterium target, with a kinematic cutoff related to the incident beam energy.

To make a quantitative separation of counts from the elastic and two-step reactions, the Monte Carlo program was used to predict the shapes of the momentum distributions of the double-arm background processes. The bremsstrahlung photon distribution was simulated using the formalism of Tsai and Whitis.[25] The number of real photons available to interact with the targets increases linearly with target length, but the end-point energy decreases through the target due to ionization energy loss. Electroproduction contributions were calculated using the equivalent radiator approximation and the same photon distribution as for externally produced photons. Pair production by one of the pion decay photons (or the Compton-scattered photon) in the target material between the interaction point and the upstream end of the target was simulated using probability distributions of Rossi.[26] Note that both the Compton and π^0 reactions have a rate dependence on target length between t^3 (real photoproduction) and t^2 (electroproduction component), compared to a linear dependence on t for elastic scattering. Therefore the ratio of background to elastic counts should increase rapidly with target length. This expectation is fulfilled by the two data points near $Q^2=2.5$ $(\mathrm{GeV}/c)^2$, although the limited statistics do not allow strong conclusions to be drawn. The spectrum taken with the 40-cm target [$Q^2=2.48$ $(\mathrm{GeV}/c)^2$] has a much larger ratio of background to elastic counts (5.0 ± 1.6 if

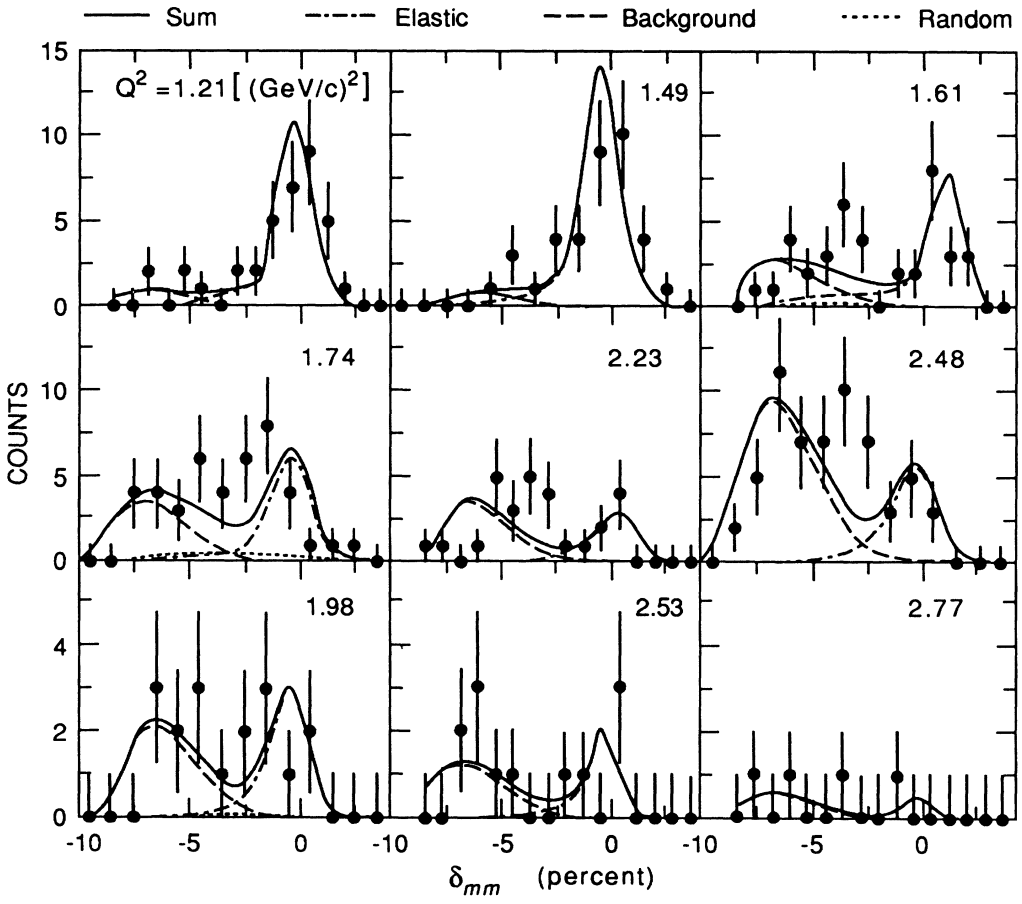

FIG. 15. Number of *e-d* coincidences as a function of missing momentum δ_{mm} at each Q^2 value of this experiment. Also shown are the two-parameter fits using Monte Carlo generated shapes for the elastic peak and background reaction, assumed to be $\gamma d \rightarrow d\pi^0$. The dot-dashed curves are the elastic contributions, the dashed curves represent the background reaction, and the dotted curves are from measured random *e-d* coincidences. The solid curves are the sums. All spectra were taken with a 20-cm long target, except at $Q^2=1.20$ $(\mathrm{GeV}/c)^2$ (10-cm target) and $Q^2=2.48$ $(\mathrm{GeV}/c)^2$ (40-cm target).

TABLE II. Results of two-parameter fits of the Monte Carlo generated elastic peak and background shapes to the *e-d* missing momenta spectra at each value of Q^2. Shown are the number N_{ed} of elastic *e-d* coincidences and χ^2 per degree of freedom values for fits assuming in the first case that the background is due to the reaction $\gamma d \rightarrow \pi^0 d$, and in the second case that the background is due to $\gamma d \rightarrow \gamma d$. Also shown is the final value for N_{ed} used to calculate the *e-d* elastic cross sections, taken as the average between the two cases. The systematic errors on N_{ed} were taken as half the difference between the results for N_{ed} for the two cases.

Q^2	Pion background		Compton background		Average	
$(\text{GeV}/c)^2$	N_{ed}	χ^2_{fit}/DOF	N_{ed}	χ^2_{fit}/DOF	$N_{ed}\pm$tot	($\pm$stat$\pm$syst)
1.20	32.1	1.14	29.8	1.08	30.9±5.7	(±5.5±1.2)
1.49	33.7	1.18	31.6	1.12	32.6±5.8	(±5.7±1.1)
1.61	24.7	1.36	20.3	1.27	22.5±5.2	(±4.7±2.2)
1.74	16.5	1.45	12.1	1.29	14.3±4.4	(±3.8±2.2)
1.98	7.2	0.98	5.1	0.88	6.2±2.7	(±2.5±1.1)
2.23	9.1	1.31	7.5	1.16	8.3±3.0	(±2.9±0.8)
2.48	15.9	1.51	10.5	1.21	13.2±4.5	(±3.6±2.7)
2.53	5.1	0.75	4.5	0.74	4.8±2.2	(±2.2±0.3)
2.77	1.2	0.37	0.9	0.36	1.1±1.1	(±1.1±0.2)

the pion background is assumed, or 3.1±0.7 for the Compton background) than the one taken with the 20-cm target [$Q^2=2.53$ $(\text{GeV}/c)^2$], where the ratio is 1.4±0.7, approximately independent of background assumption.

Since there are no cross-section measurements for either of the two-step background processes in the kinematic range of this experiment, both were considered to be equally likely to contribute to the background events. For each assumed background process, two-parameter fits to the missing momentum spectra were made, with one parameter for the magnitude of the elastic peak, and one parameter for the strength of the background. The position of the elastic peak and background end point was not free to vary, since the momentum calibration of

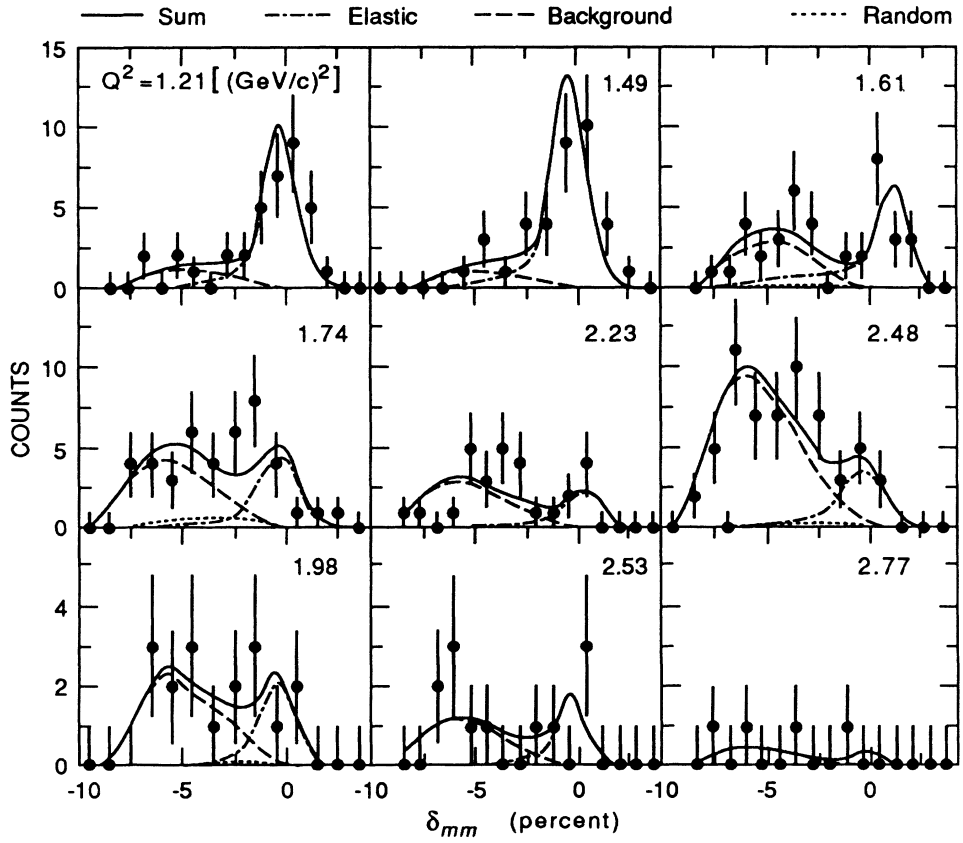

FIG. 16. Same as Fig. 15 except the background is assumed to be all due to $\gamma d \rightarrow \gamma d$.

both spectrometers was firmly established,[8] with a resulting uncertainty in δ_{mm} of only 0.25%. The shape of the elastic peak was also fixed, since the Monte Carlo accurately predicted the shapes for all the *e-p* elastic peaks, as well as the two lowest Q^2 *e-d* elastic peaks, for which there is little background. The shape and magnitude of the missing momentum distribution from random coincidences was added (with no free parameters) to the background and elastic peak shapes when performing the fits. The fits used Poisson statistics due to the small number of events. The results are listed in Table II and shown in Fig. 15 (background assumed to be π^0 production) and Fig. 16 (Compton background assumed). It can be seen in Table II that the χ^2 values are about equally good for the two background assumptions. In both cases the contribution in the elastic peak region is relatively small, so the error on the number of elastic counts is primarily determined by the number of counts in this region. Note that for almost all the data points, both elastic and background contributions are required to get a reasonable description of the spectra.

The final number of elastic coincidences was defined as the average of the results with the pion and Compton backgrounds, since both give reasonable descriptions of the spectra. The systematic error attributed to background separation was defined to be half of the difference between the Compton and pion background results. These errors ranged between 3% and 20% of the number of elastic counts. The total error was found by adding the statistical and systematic errors in quadrature, since they are uncorrelated. The cross sections calculated from the final number of counts are listed in Table III.

D. Checks of background reactions

As a check that the assumed background mechanisms are reasonable, pion photoproduction cross sections were calculated from the single-arm deuteron spectra. The assumption was made that the number of single-arm deuterons from Compton scattering was negligible, which is reasonable since the cross section for this process is expected to be at least ten times smaller, and the solid angle for single-arm deuterons is approximately the same for both reactions. Substantial corrections (30–70 %) were made for deuterons coming from the aluminum target endcaps. Since deuterons were only measured in random coincidence with an electron arm trigger, large corrections had to be made for the effective deuteron trigger efficiency. The Monte Carlo program was used to calculate the single-arm solid angle, assuming that the virtual electroproduction could be approximated by scaling the bremsstrahlung photon spectrum by an effective radiator of 0.03 r.l. thickness. The extracted c.m. cross sections, shown in Fig. 17, were found to decrease smoothly with increasing energy from 15 to 1 nb/sr. The errors are dominated by the uncertainties in the effective live time, endcap subtraction, and electroproduction factor. The 180° cross sections have approximately the same shape and magnitude as previous data[27] at 120°. Because previ-

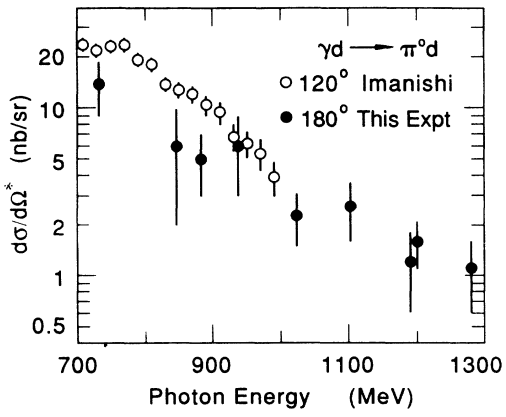

FIG. 17. Cross sections for the reaction $\gamma d \rightarrow \pi^0 d$ at a c.m. angle of 120° from Imanishi *et al.* (Ref. 27) and at 180° from this experiment. The cross sections were extracted from single-arm deuteron spectra assuming that the contribution from $\gamma d \rightarrow \gamma d$ is negligible.

TABLE III. Results of the elastic 180° electron-deuteron measurements. Given at each value of Q^2 are the number of incident electrons N_i, the target length t, the measured cross section σ_{meas}, the portion of the measured cross section due to $A(Q^2)$, and final results for $B(Q^2)$. The errors include statistical and systematic uncertainties added in quadrature.

Q^2 (GeV/c)^2	10^{-18} N_i	t (cm)	σ_{meas} (10^{-40} cm^2/sr)	$\sigma_{A(Q^2)}$ (10^{-40} cm^2/sr)	10^{18} $B(Q^2)$
1.20	0.71	10	65±12	4.6±0.5	112±22
1.49	1.85	20	14.8±2.7	1.4±0.15	34.7±7.0
1.61	3.16	20	5.6±1.3	0.86±0.12	14.0±3.8
1.74	10.4	20	1.10±0.34	0.48±0.06	2.07±1.15
1.98	12.7	20	0.38±0.17	0.20±0.02	0.75±0.71
2.23	20.5	20	0.34±0.12	0.10±0.01	1.25±0.63
2.48	22.3	40	0.31±0.11	0.035±0.006	1.67±0.66
2.53	11.0	20	0.35±0.17	0.036±0.006	2.00±1.05
2.77	12.3	20	0.07±0.07	0.020±0.003	0.36±0.54

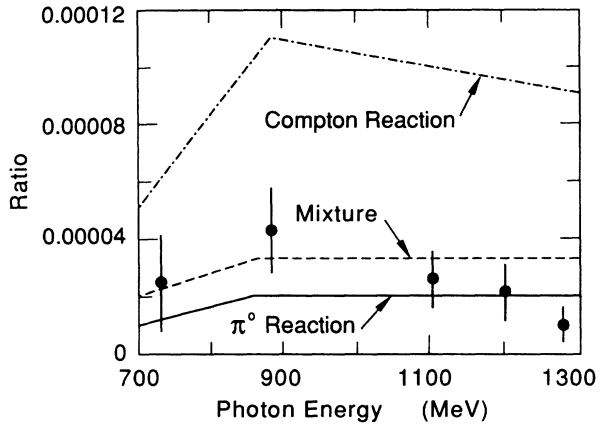

FIG. 18. Ratio of double-arm *e-d* background counts to total number of single-arm deuterons from the deuterium target. The solid (dot-dashed) curve is the prediction assuming that both single-arm and double-arm events come entirely from the π^0 (Compton) reaction. The dashed curve is the prediction if the single-arm counts are 90% from the π^0 reaction and 10% from the Compton reaction, leading to approximately equal number of counts from each reaction in the double-arm events.

ously measured angular distributions for this reaction are relatively isotropic, it is reasonable to expect that the 180° and 120° cross sections should agree within a factor of 2. The observation that they do agree within this factor supports the assumption that the single-arm deuterons principally come from the π^0 reaction.

As a further check on the assumed background reaction mechanisms, the observed ratios of background *e-d* coincidences to all single-arm deuterons were compared with the ratios calculated with the Monte Carlo program. The experimental ratios are shown in Fig. 18 at the five beam energies of NE4-II. The ratios are small, varying between one and five coincidences per 100 000 single-arm deuterons. The errors are dominated by the statistics on the number of background *e-d* coincidences and the end-cap subtraction and live-time correction for the single-arm deuterons. It can be seen that the ratios are consistent with the Monte Carlo prediction (solid curve) assuming that both single-arm and double-arm counts are due entirely to the π^0 reaction, but lie well below the prediction (dot-dashed curve) assuming that only the Compton reaction plays a role.

The data also are consistent with a prediction (dashed curve) assuming that the Compton cross section is one-tenth that of the π^0 cross section. In this case, only one-tenth of the single-arm deuterons would come from the Compton reaction, but about equal numbers of *e-d* coincidences would come from each reaction due to the much smaller detection probability for the double-arm π^0 reaction compared to the Compton reaction. These results give us confidence that the background mechanisms are understood.

E. $A(Q^2)$ contribution

To obtain final values for $B(Q^2)$ it was necessary to account for the contribution of $A(Q^2)$ due to the finite double-arm angular acceptance of the spectrometer system. The average values of $\cos^2\frac{1}{2}\theta/\sin^4\frac{1}{2}\theta$ were calculated using the Monte Carlo program and were found to be 0.0019 for the 10-cm target, 0.0018 for the 20-cm target, and 0.0015 for the 40-cm target. Using these values in Eqs. (4) and (5) and interpolating from existing data,[2] the expected cross sections due to the contribution from $A(Q^2)$ were calculated, and are listed in Table III. Equation (4) was then used again to find the final values for $B(Q^2)$. It can be seen that the portion of the measured cross sections due to $A(Q^2)$ was largest at $Q^2=1.78$ and 1.98 $(\mathrm{GeV}/c)^2$, where it accounted for half the measured values. At these Q^2 values the ratio $B(Q^2)/A(Q^2)$ becomes as low as ~ 0.002. This small ratio indicates that any future measurements in this Q^2 range will also have to be performed close to 180°.

F. Magnetic structure function of the deuteron

Final values for the elastic cross sections and extracted values of the structure function $B(Q^2)$ are listed in Table III at each of the average Q^2 values of this experiment. The errors assigned to the final cross sections include statistical and systematic contributions added in quadrature. The results for $B(Q^2)$ include the additional error in the portion of the measured cross sections due to $A(Q^2)$, also added in quadrature. The statistical errors for each data point are larger than the systematic errors, which are dominated by the uncertainty in the background separation. Other systematic errors, such as that in the target length or the double-arm solid angle, are relatively small.

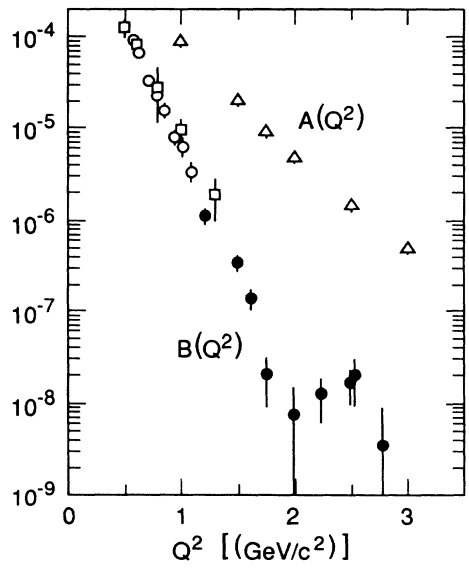

FIG. 19. Experimental values for $B(Q^2)$ from this experiment (solid circles) and previous lower Q^2 data from Auffret *et al.* (Ref. 28, open circles) and Cramer *et al.* (Ref. 29, open squares). The errors for the data of this experiment include statistical and systematic uncertainties added in quadrature. Also shown are data for $A(Q^2)$ (open triangles, Ref. 2).

The results for $B(Q^2)$, shown as the solid circles in Fig. 19, join smoothly onto previous data,[28,29] shown as open circles and squares. At higher Q^2, the new results continue to fall rapidly with increasing Q^2 until an apparent diffraction minimum is reached around $Q^2=2$ $(\mathrm{GeV}/c)^2$. The data then rise to a secondary maximum around $Q^2=2.5$ $(\mathrm{GeV}/c)^2$. It should be pointed out that $B(Q^2)$ is also consistent ($\chi^2=1.0$ per degree of freedom) with a constant value of 1.2×10^{-8} for $Q^2>1.75$ $(\mathrm{GeV}/c)^2$, although this behavior would be hard to understand theoretically. The magnitude of the cross sections in this region is very small, comparable to those for elastic neutrino scattering. Comparisons with representative theoretical models for $B(Q^2)$ will be given in the next section.

V. COMPARISON WITH THEORY

In this section a brief summary will be given of the existing theoretical models used to calculate the elastic form factors of the deuteron. The data of this experiment will be compared with representative calculations. Although the boundaries among different models are hard to define, an attempt will be made to separate them into the following categories: nonrelativistic impulse approximation (NRIA), relativistic impulse approximation (RIA), meson exchange current (MEC) and isobar (IC), hybrid quark models, the Skyrmion model, and perturbative quantum chromodynamics (PQCD).

A. Nonrelativistic impulse approximation

The NRIA is the traditional approach for the calculation of the deuteron form factors as the sum of scattering from the moving proton and neutron. In the NRIA the standard parametrization[30–32] of the electromagnetic form factors of the deuteron in terms of the electromagnetic form factors of the nucleons and the deuteron wave function has the form

$$G_C=G_E^S C_E \ , \tag{13a}$$

$$G_Q=G_E^S C_Q \ , \tag{13b}$$

$$G_M=\frac{M_d}{M_p}(G_M^S C_S+\tfrac{1}{2}G_E^S C_L) \ , \tag{13c}$$

where

$$G_E^S=G_{Ep}+G_{En} \ , \tag{14a}$$

$$G_M^S=G_{Mp}+G_{Mn} \tag{14b}$$

are the charge and magnetic isoscalar nucleon form factors. These take into account that the neutron and proton are not point currents but have their own electromagnetic form factors G_{Ep}, G_{Mp}, G_{En}, and G_{Mn}. The structure functions C_E, C_Q, C_S, and C_L for elastic electron-deuteron scattering give the distribution of the neutron and proton point currents as determined by the deuteron S- and D-state wave functions $u(r)$ and $w(r)$, respectively. They are given[32] by

$$C_E=\int_0^\infty [u^2(r)+w^2(r)]\,j_0\left[\frac{Qr}{2}\right]dr \ , \tag{15a}$$

$$C_Q=\frac{3}{\sqrt{2}\eta}\int_0^\infty w(r)\left[u(r)-\frac{w(r)}{2\sqrt{2}}\right]j_2\left[\frac{Qr}{2}\right]dr \ , \tag{15b}$$

$$C_S=\int_0^\infty \left[[u^2(r)-\tfrac{1}{2}w^2(r)]\,j_0\left[\frac{Qr}{2}\right]+\tfrac{1}{2}[\sqrt{2}u(r)w(r)+w^2(r)]\,j_2\left[\frac{Qr}{2}\right]\right]dr \ , \tag{15c}$$

$$C_L=\tfrac{3}{2}\int_0^\infty w^2(r)\left[j_0\left[\frac{Qr}{2}\right]+j_2\left[\frac{Qr}{2}\right]\right]dr \ , \tag{15d}$$

where j_0 and j_2 are spherical Bessel functions. The normalization condition is

$$\int_0^1 [u^2(r)+w^2(r)]dr=1 \ . \tag{16}$$

In the static limit ($Q^2=0$)

$$G_C=1, \quad G_Q=M_d^2 Q_d, \quad G_M=\frac{M_d}{M_p}\mu_d \ , \tag{17}$$

where μ_d and Q_d are the deuteron magnetic and quadrupole moments, respectively.

NRIA models[33,34] with various assumptions for deuteron wave functions and bound nucleon form factors pre-

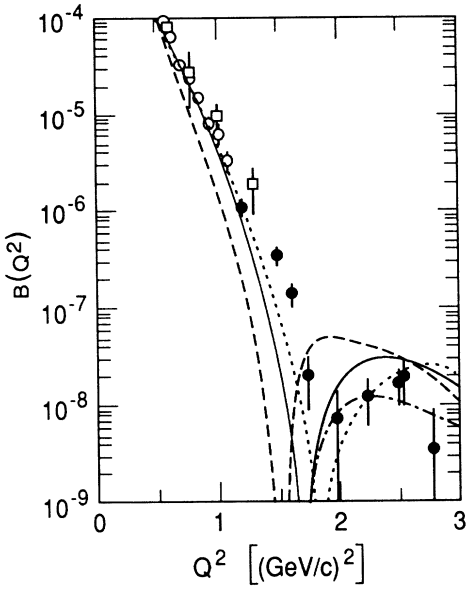

FIG. 20. Calculations from Belyantsev *et al.* (Ref. 33) for $B(Q^2)$ in the NRIA. The solid and long-dashed curves use the Paris potential, while the short-dashed and dash-dotted curves use the Muzafarov and Troitsky wave function. All curves use the dipole fit to the nucleon form factors, but the solid and short-dashed curves have $G_{En}(Q^2)=0$ while the other curves use $G_{En}(Q^2)=\tau G_{Mn}(Q^2)$. The dash-dotted and solid curves are indistinguishable below $Q^2=1.8$ $(\mathrm{GeV}/c)^2$. The open circles are from Auffret *et al.* (Ref. 28), the open squares are from Cramer *et al.* (Ref. 29), and the solid circles are from this experiment.

dict a diffractive minimum in $B(Q^2)$ somewhere between $Q^2=1.5$ and 2.0 $(\mathrm{GeV}/c)^2$. The exact location of this minimum and the height of the secondary maximum are sensitive to the short-range part of the D- and S-state wave functions. They also depend on the nucleon form factors, for which parametrizations differ considerably at large Q^2, especially for the neutron. The height of the secondary maximum generally decreases as the position of the minimum moves to higher Q^2. Figure 20 shows curves calculated[33] for two representative potentials (the Paris potential[35] and the modified dispersion approach of Muzafarov and Troitsky[30]) and two parametrizations of the nucleon form factors. Both parametrizations use the dipole fit for G_{Mp}, G_{Mn}, and G_{Ep}, but in one case $G_{En}=0$ and in the other $G_{En}=\tau G_{Mn}$ (where $\tau=Q^2/4M_p^2$), reflecting two extremes consistent with the limited data on $G_{En}(Q^2)$. It can be seen that the NRIA calculations reasonably describe the principal features of the data, but all fall below the data in the region $1.2<Q^2<1.8$ $(\mathrm{GeV}/c)^2$, corresponding to a predicted minimum at too low values of Q^2. The use of other realistic potentials [such as the Reid soft core[36] (RSC)] does not solve this problem.[34] On the other hand, the magnitude of the secondary maximum is in reasonable agreement with the data. It can be seen in Fig. 20 that the choice of potential and nucleon form factor parametrization can have an equally large influence on the predictions. As new data become available,[37] the uncertainty in nucleon form factors will be reduced, thus reducing the range of inputs to the models for $B(Q^2)$.

B. Relativistic impulse approximation

In relativistic calculations a choice must first be made as to whether the dynamic variables represent the particles or the fields. The latter approach, exemplified by quantum hydrodynamics, has considerable difficulties for short-distance phenomena, and will not be discussed further here. For the choice of particles being represented by the dynamical variables, a further choice can be made as to whether to construct a Hamiltonian that develops the system along an axis perpendicular to the light-front (light-front quantum mechanics) or along the time axis (the so-called "instant" forms).

A good example using the instant form is the relativistic impulse approximation (RIA) calculation of Arnold, Carlson, and Gross,[38] which solves the Bethe-Salpeter equation and uses a four-component deuteron wave function. The kinematics are treated relativistically to all orders in $(v/c)^2$, but the approximation is made that the spectator nucleon is on shell, only allowing the interacting nucleon to be off shell. The relevant Feynman diagrams are shown in Fig. 21. The covariant diagram of Fig. 21(a) includes the three time-ordered diagrams of Fig. 21(b), allowing for the inclusion of the pair current term where the photon splits into an $N\bar{N}$ pair. As for all the other relativistic calculations discussed in this section, the meson-exchange currents (MEC's) [Fig. 21(c)] and isobars [Fig. 21(d)] have not been included. The deuteron nucleon-nucleon vertex is described by four in-

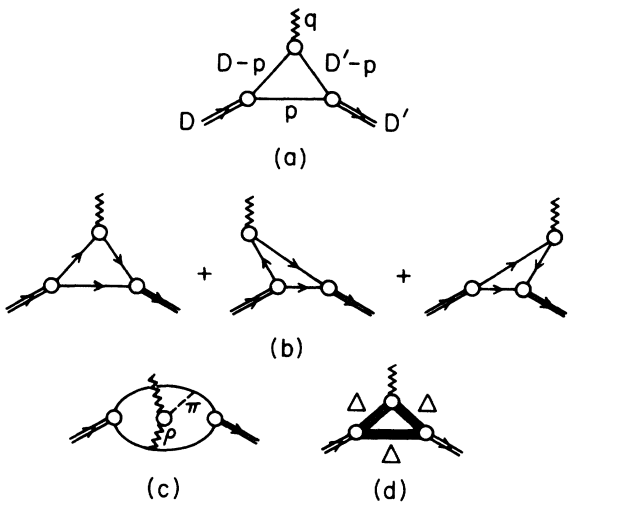

FIG. 21. (a) The relativistic Feynman diagram which describes the impulse approximation (RIA). (b) Three nonrelativistic time-ordered diagrams included in the RIA. The lines moving backwards in time are antiparticles. (c) Meson exchange contribution. (d) Isobar diagram. Diagrams (c) and (d) are not included in the RIA.

variants which are the familiar S- and D-state wave functions of the NRIA plus two additional P-state wave functions. While the P states contribute a negligible portion to the overall wave function, their contribution at high momentum can be large in the momentum space representation. The wave functions were determined from relativistic one-boson exchange models with π, σ, ρ, and ω exchange and a mixture of couplings determined by a parameter λ such that the coupling is pure γ^5 for $\lambda=1$ and pure $\gamma^5\gamma^\mu$ with $\lambda=0$. It turns out that the strength of the P-state components increases linearly with λ. The results for the RSC potential and dipole form factors are shown in Fig. 22 for three values of λ. It can be seen that in all cases the predicted minimum is shifted to lower Q^2 compared to the NRIA calculation (solid curve), with the shift being largest for $\lambda=1$. This results in worse agreement with the data for $B(Q^2)$. The agreement with the data for $A(Q^2)$ is also worse using this relativistic approach. It is not known whether the inclusion of two-body currents could shift the predictions back towards the data.

The Gross approximation[38] to the Bethe-Salpeter equation has also been investigated extensively by Zuilhof and Tjon[39] using a one-boson exchange potential. They found the most important corrections to the static limit come from boosts on the one-particle propagators and confirmed that the relativistic results shift the diffraction minimum to lower Q^2 values than the nonrelativistic results. Zuilhof and Tjon also investigated the influence of isoscalar MEC's, finding that such contributions should not be large.

Gurvitz and Bhalero[40] calculated the deuteron form factors in the ladder approximation to the Bethe-Salpeter equation, and discovered that the most important relativistic kinematical effect is the shift in the p-n relative

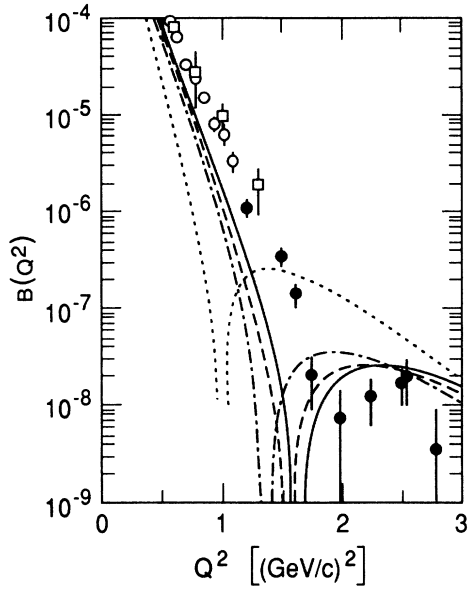

FIG. 22. Predictions for $B(Q^2)$ in the RIA from Arnold *et al.* (Ref. 38) using dipole nucleon form factors and $G_{En}(Q^2)=0$. The curves are for $\lambda=0$ (dashed), $\lambda=0.4$ (dash-dotted), and $\lambda=1$ (dotted). Shown for comparison is a calculation in the NRIA with the RSC potential (solid curve). The data are the same as in Fig. 20.

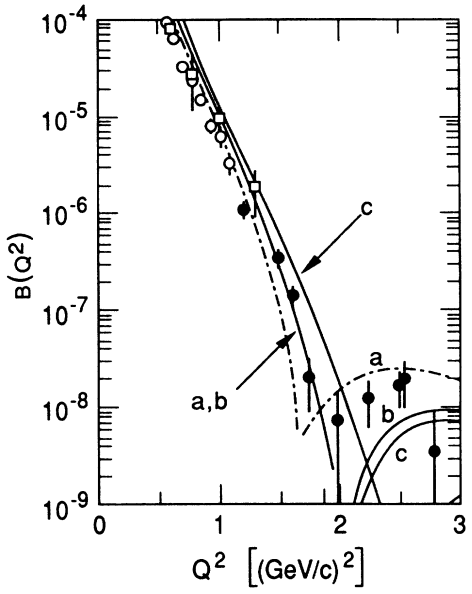

FIG. 23. Relativistic predictions for $B(Q^2)$ of Bhalero and Gurvitz (Ref. 40) using the (a) Paris, (b) Reid soft-core, and (c) Hamada-Johnston hard core (Ref. 41) nucleon-nucleon interaction. The dot-dashed curve is the nonrelativistic result using the Paris wave function. Dipole form factors are used with $G_{En}(Q^2)=0$. The data are the same as in Fig. 20.

momentum due to the Lorentz transformation to the deuteron rest frame. Relativistic calculations with the spectator (struck) nucleon on mass shell result in values for $A(Q^2)$ which are lower (higher) than those obtained nonrelativistically. This occurs because these two prescriptions lead to *p-n* relative momenta in the deuteron rest frame which are, respectively, higher and lower than the nonrelativistic case (see Fig. 1 of Ref. 40). To avoid this sensitivity to the choice of on-shell nucleon, Gurvitz and Bhalero construct a symmetrical form as a sum of two components, each with one of the two nucleons on mass shell. The Lorentz boost thus defined shifts the *p-n* relative momentum and causes an effect which increases with Q^2. Their predictions for $B(Q^2)$ using three different deuteron wave function models are compared with the data in Fig. 23. It can be seen that, for a given potential, the relativistic calculation now shifts the diffraction minimum to higher momentum transfer than the nonrelativistic one. Reasonable agreement with the data is found for both the realistic Paris[35] and RSC (Ref. 36) potentials, but the Hamada-Johnston hard core potential[41] shifts the minimum to Q^2 values that are much too high. The same authors find good agreement with the data for $A(Q^2)$, with the relativistic results larger than the nonrelativistic ones. In contrast, Arnold *et al.*[38] and Zuilhof and Tjon[39] find the opposite trend.

Several relativistic calculations have been performed using light-cone dynamics. A significant advantage of this approach is that Lorentz transformations (such as the boost needed to go from the moving frame of an electron-deuteron collision to the static frame in which the deuteron wave function is defined) do not depend on the strong interaction. This considerably simplifies the calculation of the one-body current matrix elements. In particular, the nucleon form factors needed can be unambiguously identified with the free, experimentally measured form factors. Another advantage is that the equation of motion that results from this approach has the same form as the nonrelativistic Schrödinger equation, so that the same wave functions can be used as in the nonrelativistic case. The difference is that the wave functions are not evaluated at the same momenta as in the nonrelativistic case. The treatment of two-body currents is not simplified compared to the "instant" form, and has not yet been attempted.

The results for the light-front model of Chung *et al.*[42] are shown in Figs. 24(a) and 24(b). Since no MEC or isobar contributions were included, the principal theoretical uncertainties were the choice of deuteron wave function and nucleon form factor parametrization. It can be seen that the minima have moved to slightly higher Q^2 than for NRIA calculations with the same wave functions, in better agreement with the data. As in the NRIA case, the minima occur at lower Q^2 for the wave functions with lower *D*-state probability such as Bonn *R* and Bonn *E*.[43] The choice of nucleon form factors can be as important as the choice of wave function, as can be seen by comparing the results in Fig. 24(a) [the Gari-Krümplemann (GK) parametrization[24]] with those in Fig. 24(b) (Höhler parametrization[22]). The GK form factors differ from most other commonly used parametriza-

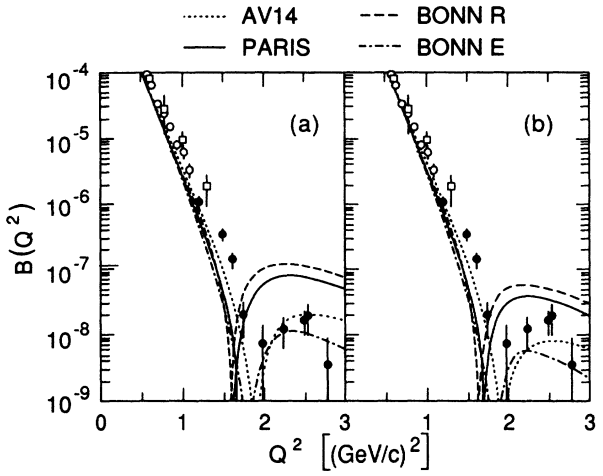

FIG. 24. Relativistic calculations for $B(Q^2)$ of Chung *et al.* (Ref. 42) for different deuteron wave functions using (a) GK, and (b) Höhler nucleon form factors. The data are the same as in Fig. 20.

tions in that the neutron Dirac structure function F_{1N} is close to zero, which means that $G_{En}(Q^2)$ grows with Q^2 and $G_{Mn}(Q^2)$ falls off considerably faster with increasing Q^2 than the dipole fit. As has been seen in NRIA calculations, the Chung results slightly favor the GK form factors for fitting the $B(Q^2)$ data between $Q^2=1$ and 1.8 $(\mathrm{GeV}/c)^2$, with the best agreement being found for the AV14 potential,[44] although even this curve falls considerably below some of the data points. Chung *et al.* found good agreement with the data for $A(Q^2)$ for this potential and the GK form factors.

Light-front dynamics have also been used by Grach and Kondratyuk[45] and Frankfurt and Strikman.[46] Although they use different methods to calculate the structure function formulas, the basic approximations made are the same (for example only keeping the so-called good components of the electromagnetic current), and the final results from both papers agree. The results also appear to be similar to those of Chung *et al.*, but it is not clear if all the same basic approximations were made. Kondratyuk, Grach, Frankfurt, and Strikman have shown in a recent paper[47] that the diffraction feature seen in the data near $Q^2=2$ $(\mathrm{GeV}/c)^2$ is well explained by light-cone quantum mechanics without the need for significant two-body currents, and provides evidence for a nuclear core to the deuteron.

C. Meson-exchange currents and isobar contributions

As seen above, the calculations based on the NRIA tend to give results which fall below the data for Q^2 larger than ~ 1.2 $(\mathrm{GeV}/c)^2$, although much better agreement is achieved for some choices of the deuteron wave function and nucleon form factors than for others. Relativistic calculations improve or worsen the agreement, depending on the approach taken. It has long been recognized that the inclusion of meson-exchange diagrams and diagrams involving isobars should not be neglected. While they have not yet generally been included in relativistic calculations, they have been used by many authors to augment the NRIA.

First-order MEC and isobar contribution diagrams are shown in Fig. 25. Diagram (a) is associated with the derivative nature of the meson-nucleon vertices; (b) involves intermediate antinucleon states (pair currents); (c) corresponds to the direct coupling of the photon to the mesons, an isovector process not allowed in *e-d* elastic scattering; (d) involves nucleon excited states; and (e) is very important for magnetic isoscalar transitions such as in *e-d* elastic scattering. In addition to diagrams like that in Fig. 25(d), isobar contributions can arise from various $\Delta\Delta$ configurations in the deuteron wave function.

Initial calculations[48] that included isoscalar MEC's found the diffraction minimum to be completely filled in, and the magnitude of the cross section to increase noticeably, in strong disagreement with the data of this experiment, when standard potentials such as the Paris or RSC were used (see, for example, Figs. 12 or 22 of Ref. 48). The dominant MEC contributions come from the pair current and the $\rho\pi\gamma$ term. The latter is sensitive to the strength of the $\rho\pi\gamma$ coupling constant, whose presently accepted value[49] of 0.56 is not well established experimentally.

More recent calculations[50,51] also show that the inclusion of MEC's pushes the predictions above the data when the Paris or RSC potentials are used, but that good agreement with the data can be found for other potentials. For example, Dymarz and Khanna[50] find that for potentials MD and W1, which have $\approx 0.3\%$ Δ-isobar probability, the NRIA predicts a minimum at much lower Q^2 than indicated by the data, but inclusion of the MEC's brings the calculations into good agreement with the data. Calculations with their W2A, W2B, and W3 models (with isobar probabilities of 0.47, 0.65, and 0.88%, respectively) either have the minimum at too high Q^2, or find the minimum missing entirely. Dymarz and

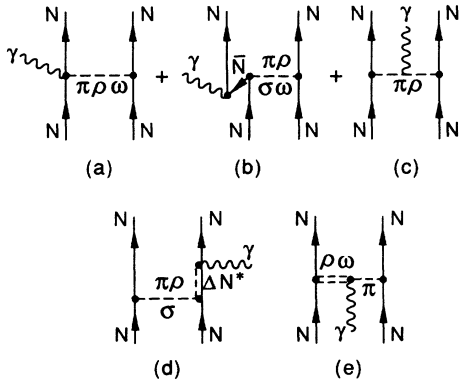

FIG. 25. First-order MEC's. (a) Seagull, (b) pair, (c) mesonic, (d) isobaric, and (e) "$\rho\pi\gamma$" and "$\omega\pi\gamma$" diagrams.

Khanna have investigated both the effect of the nucleon form factor parametrizations as well as the effect of the assumed Δ form factor. For models with large isobar probabilities, the latter can be very important.

The importance of MEC and isobar configurations was also investigated extensively by Sitarski *et al.*[51] using six deuteron potential models. These calculations use *R*-matrix theory and a coupled-channel approach that includes $6q$ components inside of a radius r_0 (see the discussion of hybrid quark models below). They find that the data for $B(Q^2)$ are particularly useful in determining the ratio of $^7D_1$ to $^3D_1$ ΔΔ states, with the total *D*-state ΔΔ strength determined by fits to *NN* scattering data. Adjusting the ratio ΔΔ states to fit $B(Q^2)$ at $Q^2<1$ $(\mathrm{GeV}/c)^2$, Sitarski *et al.* extrapolated to higher Q^2 as shown in Fig. 26. Potential model *C'* has a small nucleon bag radius of 0.74 fm and a Δ percentage of 1.76%, while model *D'* has a larger nucleon bag radius of 1.05 fm and a Δ percentage of 7.2%. If interpreted as physical states, these ΔΔ strengths are rather large compared to an upper limit of 0.4% obtained in a recent neutrino experiment.[52] In any case, it can be seen that both models *C'* and *D'* are in good agreement with the high-Q^2 data for $B(Q^2)$ when GK nucleon form factors are used, but fall below the secondary maximum when the Höhler parametrization is used.

D. Hybrid quark models

While the long- and medium-range nuclear force can be reasonably well understood in terms of virtual meson exchange, the short-range part is more problematic. At distances significantly less than the nucleon size of about 1 fm, the internal structure of the nucleons (quarks and gluons) is likely to play a role. An attempt to treat the nucleus entirely as a system of quarks rather than nucleons is given by Matveev and Sorba.[53] This approach has difficulty in describing the low-momentum deuteron properties and is not yet useful for practical calculations. It has proven more effective to invent so-called "hybrid models," in which the quark structure becomes important only inside a certain radius or above a certain momentum. The calculations of Sitarski *et al.*[51] discussed above are a good example of this approach using the coupled-channel formalism. As was seen, the data for $B(Q^2)$ could be well described using potentials with either a large or small bag radius.

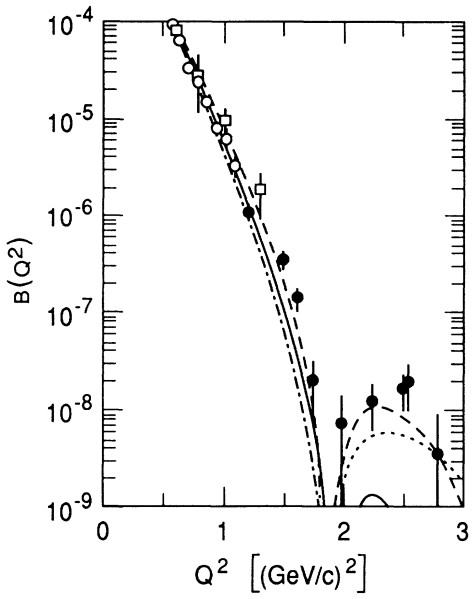

FIG. 26. Nonrelativistic predictions including MEC, IC, and $6q$ states of Sitarski *et al.* (Ref. 51) using potential model *C'* with nucleon form factor parametrizations of Höhler (solid) and GK (dashed), and for model *D'* using Höhler (dash-dotted) and GK (dotted). The dotted and solid curves are indistinguishable below the diffraction minimum. The data are the same as in Fig. 20.

An earlier calculation along similar lines[54] obtained the *n-p* system form factors with the RSC potential[36] in the impulse approximation, using a nonrelativistic three-dimensional oscillator model for the $6q$ configuration. The two unknown parameters in the model, namely the probability β of the $6q$ state in the deuteron and the parameter ω of the oscillator potential, were determined by fitting the data for $B(Q^2)$ for $Q^2\leq 1$ $(\mathrm{GeV}/c)^2$. The fits were insensitive to the choice of nucleon form factors and oscillator model. For $Q^2>1$ $(\mathrm{GeV}/c)^2$, where the difference between these fits becomes appreciable, the $6q$ state begins to dominate the other contributions to $B(Q^2)$. With the free parameters determined, the prediction for $B(Q^2)$ overestimates the new data by an order of magnitude at $Q^2=2$ $(\mathrm{GeV}/c)^2$, the highest Q^2 value calculated.

Yamauchi *et al.*[55] derive a model of the nucleon-nucleon interaction within the framework of the nonrelativistic quark cluster theory based on the resonating group method (RGM). By correctly taking into account the effect of the quark exchange between two different nucleons, the model smoothly connects the two-nucleon configuration at long distances to the $6q$ configuration at short distances. The model is constructed so as to incorporate not only the quark- and gluon-exchange mechanism at short distances, but also the meson-exchange mechanism at long and intermediate distances. The MEC contributions were neglected for the elastic form factors of the deuteron because they are of the isoscalar type and their treatment is much more involved and uncertain. The prediction of this model does not cover the entire Q^2 range of this experiment and increasingly underestimates the magnetic structure function, as shown by the solid curve in Fig. 27. Based on the results discussed above, it is likely that the inclusion of MEC's would improve the agreement with the data.

Another approach based on the RGM was developed by Chemtob and Furui,[56] and is formulated in momentum space representation rather than in configuration space, as was done by Yamauchi *et al.* The two-baryon system is described as a composite of six equivalent quarks whose states are represented in terms of a three-quark cluster basis and where the interaction mechanisms consist of quark interchange effects, gluon exchange, perturbative corrections, and pion exchange effects. The

Paris[35] and the RSC (Ref. 36) potentials were used, expressed as superpositions of Yukawa-type wave functions.[57] The results obtained with the Paris wave function and a momentum-dependent normalization are shown in Fig. 28(a). It can be seen that the sum of the impulse [with dipole form factors and $G_{En}(Q^2)=0$] and quark-exchange contributions gives a minimum at too low Q^2, while the inclusion of the $\rho\pi\gamma$ exchange current (with $g_{\rho\pi\gamma}=0.4$) provides much better agreement with the data. Contributions from the isoscalar pion pair current were not included. On the other hand, the neglect of the $\rho\pi\gamma$ diagram but use of $G_{En}(Q^2)=-\tau G_{Mn}(Q^2)$ for the impulse term also moves the prediction much closer to the data. Figure 28(b) shows the predictions again using the Paris wave function but now with constant normalization. For all three curves, the minimum is now shifted to higher Q^2 compared to using momentum-dependent normalization. In this case the curve neglecting the MEC diagram and using $G_{En}(Q^2)=0$ agrees best with the data. It can be seen that the choice of normalization, the influence of the $\rho\pi\gamma$ diagram, and the choice for $G_{En}(Q^2)$ all have equally dramatic effects on the predictions.

The quark compound bag (QCB) model of Bakker and Dijk[58] also incorporates quark degrees of freedom in the description of the deuteron. In this approach the quark degrees of freedom manifest themselves as confined multiquark states. The model incorporates semiphenomenological coupling between the hadronic clusters for interhadronic distances $r \geq b$, and multiquark states for $r < b$, where the value of b is related to the size of the $6q$ states. The strength of the coupling is calibrated by a fit[59] to NN scattering data. A calculation of Bakker and Dijk using the GK (Ref. 24) nucleon form factor parametrization, and a quark counting rule based pentapole form for the $6q$ state form factor, is in good agreement with the data, as shown by the dashed curve in Fig. 27. Good agreement with the data for $A(Q^2)$ is also found with these assumptions.

The hybrid quark-hadron model of Kisslinger *et al.*[60] for elastic electron-deuteron scattering combines the impulse approximation, pion pair currents, and $6q$ contributions. The two-nucleon description is used for relative distances $r \geq R_B$ (where R_B is the $6q$ bag radius), while for distances $r < R_B$ the system is treated as six quarks constrained to move within a single spherical confinement region. The $6q$ probability is defined as the overlap integral of the $6q$ wave function inside the boundary radius, and is quite sensitive to the value of R_B, estimated to be between 0.8 and 1.6 fm. The contribution of the $6q$ cluster is largest for small values of this radius. For $B(Q^2)$, the $6q$ contribution becomes dominant for $Q^2 > 0.6$ (GeV/c)^2. It will be interesting to compare this model to the data once the calculations are extended beyond $Q^2 = 1.2$ (GeV/c)^2.

Honzawa *et al.*[61] investigated the deuteron form factors in the framework of the covariant oscillator quark model by assuming a $6q$ cluster component in the core region in addition to the standard NN component. This model predicts smooth asymptotic behavior for both $A(Q^2)$ and $B(Q^2)$ [in good agreement with $A(Q^2)$], which is excluded by the diffraction minimum seen in the data of this experiment.

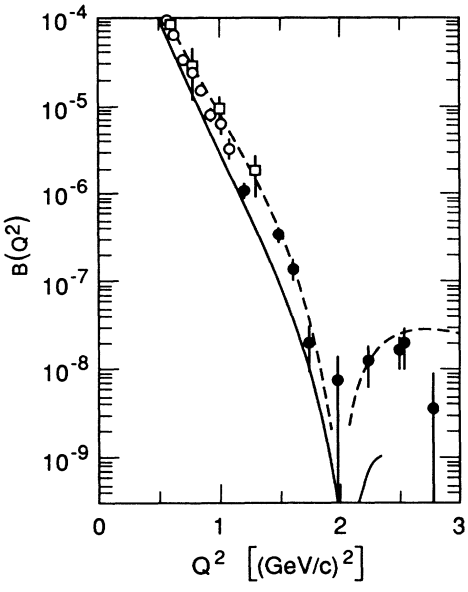

FIG. 27. $B(Q^2)$ in the resonating group model of Yamaauchi *et al.* (Ref. 55, solid curve) and in the quark compound bag model of Bakker and Dijk (Ref. 58, dashed curve). The data are the same as in Fig. 20.

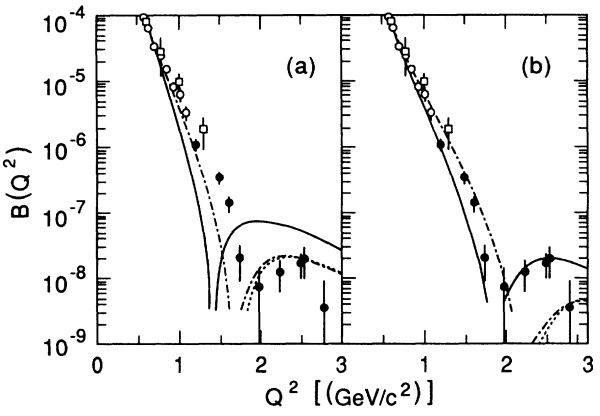

FIG. 28. $B(Q^2)$ in the model of Chemtob and Furui (Ref. 56) calculated (a) with the Paris wave function and momentum-dependent normalization. The solid curve is the sum of the impulse diagrams [with $G_{En}(Q^2)=0$] and quark exchange. The dot-dashed curve is the sum of the impulse, quark exchange, and the $\rho\pi\gamma$ exchange current (the isoscalar pion pair current is not included). The dotted curve is the same as the dot-dashed curve but with $G_{En}(Q^2)=-\tau G_{Mn}(Q^2)$. (b) Same as (a) but using constant, momentum-independent normalization. The dot-dashed and dotted curves are indistinguishable to the left of the diffraction minimum. The data are the same as in Fig. 20.

E. Skyrmion model

In the early 1960s, Skyrme[62] proposed a unified model of hadrons constructed uniquely of Goldstone meson fields (referred to as chiral fields) that could describe both mesons and baryons. The manner in which baryons emerged from a Lagrangian containing meson fields only was highly unconventional; the spin arose from scalar fields via a topological twist. Witten[63] updated Skyrme's idea by linking the Skyrme soliton solutions (Skyrmions) to QCD. He showed that at large N_c (where N_c is the number of colors) QCD leads to an effective Lagrangian of the Skyrme type and the baryons emerge as solitons from the effective theory. The topological quantum number is identified with the baryon number. The current operator B^μ depends only on the fields of the Lagrangian and not on their interactions, and can be expressed[62] in terms of an SU(2) field U as

$$B^\mu=\frac{\epsilon^{\mu\nu\alpha\beta}}{24\pi^2}\mathrm{Tr}[U^\dagger\partial_\nu UU^\dagger\partial_\alpha UU^\dagger\partial_\beta U] \ . \tag{18}$$

For the single nucleons the topological soliton field $U(r)$ has the hedgehog form

$$U(\mathbf{r})=\exp\{i\tau\cdot\hat{\mathbf{r}}\vartheta(r)\} \ , \tag{19}$$

where the function $\vartheta(r)$ (the chiral angle) satisfies an equation of motion which, in principle, is derivable from the Lagrangian. Since the form of the current operator Eq. (18) does not depend on the Lagrangian, the anomalous current can be calculated if the chiral angle ϑ is known.

Nyman and Riska[64] calculated the form factors of the deuteron by determining the chiral angle ϑ from the electromagnetic structure of the individual nucleons and using this function to predict the isoscalar exchange current in the two-nucleon case. They made the product assumption that

$$U(\mathbf{r}_1,\mathbf{r}_2;\mathbf{r})=U(\mathbf{r}-\mathbf{r}_1)U(\mathbf{r}-\mathbf{r}_2) \ , \tag{20}$$

where $\mathbf{r}_1$ and $\mathbf{r}_2$ are the coordinates of the centers of the two solitons, and $\mathbf{r}$ is the point of interaction with the electromagnetic field. With this ansatz the baryon current splits into a one-body current for each nucleon and an exchange current operator. Figure 29 shows the prediction (solid curve) for $B(Q^2)$ obtained when the chiral angle is determined by the dipole form of the isoscalar electric form factor of the nucleon. This prediction is in reasonable agreement with the data. Shown in the same figure is the curve obtained using the chiral angle given by the GK (Ref. 24) parametrization for G_E^S (dashed curve). For this case the minimum is predicted to be at too large a value of Q^2. If the chiral angle of the Skyrme model is used,[65] the magnetic form factor prediction is about a factor of 2 larger than the data at large momentum transfers.

Braaten and Carson[66] argue that the use of the product ansatz has been discredited by the discovery that it does not probe the lowest-energy configurations of the two-baryon system, and that the separation of the form factor into impulse and exchange contributions is unnatural in a soliton model. Their treatment using the semiclassical minimal-energy solution gives a diffraction minimum for $B(Q^2)$ at 1.4 $(\mathrm{GeV}/c)^2$, and is several orders of magnitude larger than the data for $Q^2>2$ $(\mathrm{GeV}/c)^2$. However, these authors are encouraged that this "pure" Skyrme model calculation shows the same qualitative features as the data.

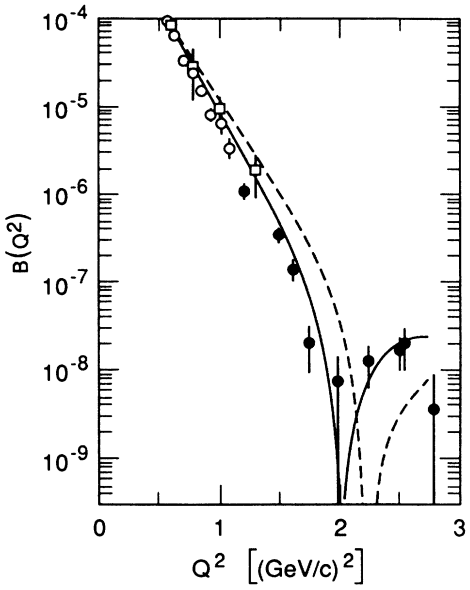

FIG. 29. $B(Q^2)$ in the Skyrmion model (Ref. 64). The two curves were obtained using the dipole (solid) and GK (Ref. 24, dashed) chiral angle parametrization for G_E^S. The data are the same as in Fig. 20.

F. Perturbative quantum chromodynamics

As expressed previously, a description of the deuteron in terms of nucleons and mesons seems to work well at low-momentum transfers [below $Q^2\sim1$ $(\mathrm{GeV}/c)^2$]. At moderate Q^2 [1–3 $(\mathrm{GeV}/c)^2$] the inclusion of explicit $6q$ states inside of a certain radius is allowed by the present data, but not necessarily required, depending on the assumptions made in the calculations. At very high Q^2, the short-range description of the deuteron should dominate, and the form factors should be describable in terms of QCD diagrams involving only quarks and gluons. At sufficiently high Q^2, the strong coupling constant, which decreases logarithmically with Q^2, should become small enough that only the leading order diagrams need be considered. One of the current challenges is to determine the Q^2 range where these concepts become valid.

While numerical predictions are not yet available, the Q^2 dependence of the deuteron form factors has been calculated[67] in leading order PQCD. A minimum of five gluon exchanges are needed to bind the final-state deuteron. This implies that the charge form factor should fall off as Q^{-10} (one power of Q^2 for each gluon exchange), and therefore $A(Q^2)$ should fall off as Q^{-20}. Due to the extra helicity flip needed, the magnetic form factor should fall off as an extra power of Q^2, and $B(Q^2)$ should

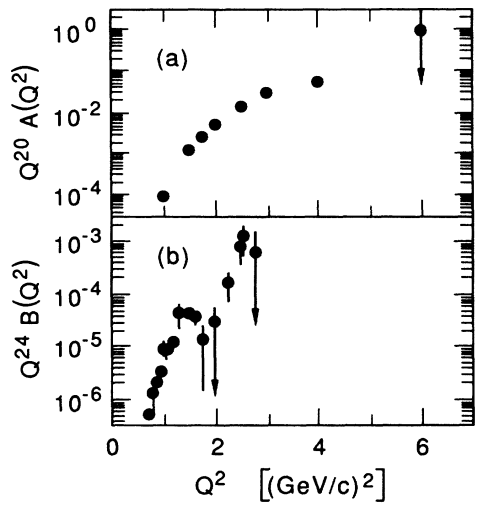

FIG. 30. Data for (a) $Q^{20}A(Q^2)$ from Ref. 2 and (b) $Q^{24}B(Q^2)$ from this experiment and Refs. 28 and 29. In leading-order PQCD, these quantities should approach a constant value at high Q^2.

decrease as Q^{-24}. To determine if the existing data approach the predicted asymptotic Q^2 dependence, the results for $Q^{20}A(Q^2)$ and $Q^{24}B(Q^2)$ are shown in Fig. 30. It can be seen that the diffraction minimum in $B(Q^2)$ at $Q^2 \sim 2$ (GeV/c)^2 is clearly inconsistent with asymptotic behavior, while there is evidence that $Q^{20}A(Q^2)$ may be flattening out at the highest Q^2. Both higher Q^2 data and more detailed theoretical investigations will be needed before the minimum Q^2 for the applicability of perturbative QCD to deuteron form factors can be determined.

VI. SUMMARY

In summary, it has been found that the lack of knowledge of the high-Q^2 behavior of the nucleon form factors and the high-momentum components of the deuteron wave function make it difficult to make unambiguous predictions for the deuteron elastic form factors, even in the NRIA. The situation will improve in the future with new measurements of the nucleon form factors and improved NN scattering data. Even with the large range of wave functions and nucleon form factor parametrizations available, most predictions for $B(Q^2)$ give a minimum that is too low in Q^2. Considerable improvement is provided by some relativistic calculations, in particular those using light-front dynamics. Other relativistic approaches shift the minimum to even lower Q^2 than the NRIA. Work is in progress to understand this problem and to reduce the ambiguities in these calculations.

While MEC and isobar diagrams have not yet been calculated relativistically, they generally are found to push the diffraction minimum to higher Q^2, in better agreement with the data, although for some potentials the minimum is pushed *too* high. Theoretical uncertainties include the strength of the $\rho\pi\gamma$ coupling constant and the allowed admixtures of $\Delta\Delta$ states in the deuteron wave function. Hybrid models have been developed to include $6q$ states in the interior and to describe the high-momentum part of the deuteron wave function. Considerable uncertainty exists about the form these $6q$ states should take, and how to treat the boundary with the ordinary NN configuration. Nonetheless, some models find good agreement with the present data for $B(Q^2)$ as well as the data for $A(Q^2)$, NN scattering data, and static deuteron properties. Interestingly, the Skyrme approach, usually used to describe low-energy phenomena, provides another way to calculate two-body currents, and one calculation using a product ansatz describes the data for $B(Q^2)$ quite well. Finally, PQCD predicts the onset of asymptotic power-law dependence for the form factors at high Q^2. It is clear from the data of this experiment that $Q^2 = 3$ (GeV/c)^2 is not high enough, at least for elastic scattering.

ACKNOWLEDGMENTS

We gratefully acknowledge the support of J. Davis, R. Eisele, C. Hudspeth, J. Mark, J. Nicol, R. Miller, and the rest of the SLAC staff. This work was supported in part by Department of Energy Contracts DE-AC03-76SF00515 (SLAC), W-7405-ENG-48 (LLNL), and DE-AC02-76ER02853.A013 (University of Massachusetts); National Science Foundation Grant No. PHY85-10549 (American University); and the U.S.-Israel Binational Science Foundation (Tel Aviv).

*Present address: Department of Physics, Princeton University, Princeton, NJ 08544.

†Permanent address: Department of Physics, Georgetown University, Washington, DC 20057.

‡Present address: Department of Physics, University of Rochester, Rochester, NY 14627.

§Permanent address: School of Physics, Shizuoka University, Shizuoka, 422 Japan.

[1]R. G. Arnold *et al.*, Phys. Rev. Lett. **61**, 806 (1988).

[2]R. G. Arnold, B. T. Chertok, E. B. Dally, A. Grigorian, C. L. Jordan, W. P. Schutz, R. Zdarko, F. Martin, and B. A. Mecking, Phys. Rev. Lett. **35**, 776 (1975).

[3]B. Grossetête, D. Drickey, and P. Lehmann, Phys. Rev. **141**, 1425 (1966).

[4]R. E. Rand, R. F. Frosch, C. E. Littig, and M. R. Yearian, Phys. Rev. Lett. **18**, 469 (1967).

[5]A. T. Katramatou, Stanford Linear Accelerator Center Report SLAC-NPAS-TN-86-8, 1986.

[6]R. G. Arnold *et al.*, Phys. Rev. Lett. **58**, 1723 (1987).

[7]A. T. Katramatou, Ph.D. thesis, American University, 1988.

[8]A. T. Katramatou, G. Petratos, R. G. Arnold, P. Bosted, R. L. Eisele, and R. Gearhart, Nucl. Instrum. Methods **A267**, 448 (1988).

[9]G. G. Petratos, Ph.D. thesis, American University, 1988.

[10]R. F. Koontz, Proceedings of the Linear Accelerator Conference, Darmstadt, West Germany; 1984, Stanford Linear Ac-

celerator Center Report SLAC-PUB-3329, 1984.
[11]R. B. Neal, *The Stanford Two-Mile Accelerator* (Benjamin, New York, 1968).
[12]R. C. Walker *et al.*, Phys. Lett. B **224**, 353 (1989).
[13]R. S. Larsen and D. Horelick, in *Proceedings of the Symposium on Beam Intensity Measurement,* Daresbury, 1968, edited by V. W. Horton and S. A. Lowndes (Daresbury Nuclear Physics Laboratory, Daresbury, Lancashire, England, 1968).
[14]P. Bosted and A. Rahbar, Stanford Linear Accelerator Center Report NPAS-TN-85-1, 1985.
[15]M. J. Brown, C. Granieri, D. J. Sherden, and L. Weaver, Stanford Linear Accelerator Center Report SLAC-PUB-2494, 1980.
[16]W. N. Hess, Rev. Mod. Phys. **30**, 368 (1958); V. S. Barashenkov and V. M. Maltev, Fortschr. Phys. **9**, 549 (1961).
[17]M. Aguilar-Benitez *et al.*, Phys. Lett. **170B**, 1 (1986).
[18]W. Bartel, F. W. Büsser, W.-R. Dix, R. Felst, D. Harms, H. Krembiel, P. E. Kuhlmann, J. McElroy, J. Meyer, and G. Weber, Nucl. Phys. B **58**, 429 (1973).
[19]Ch. Berger, V. Burkert, G. Knop, B. Langenbeck, and K. Rith, Phys. Lett. **35B**, 87 (1971).
[20]J. Litt *et al.*, Phys. Lett. **31B**, 40 (1970).
[21]T. Janssens, R. Hofstadter, E. B. Hughes, and M. R. Yearian, Phys. Rev. **142**, 922 (1966).
[22]G. Höhler, E. Pietarinen, I. Sabba Stefanescu, F. Borkowski, G. G. Simon, V. H. Walther, and R. D. Wendling, Nucl. Phys. **B114**, 505 (1976), Fit 5.3 (proton) and Fit 8.2 (neutron).
[23]F. Iachello, A. D. Jackson, and A. Lande, Phys. Lett. **43B**, 191 (1973).
[24]M. Gari and W. Krümpelmann, Phys. Lett. B **173**, 10 (1986); Z. Phys. A **322**, 689 (1985).
[25]Y. S. Tsai and V. Whitis, Phys. Rev. **149**, 1248 (1966).
[26]B. Rossi, *High Energy Particles* (Prentice-Hall, Englewood Cliffs, NJ, 1961).
[27]A. Imanishi *et al.*, Phys. Rev. Lett. **54**, 2497 (1985).
[28]S. Auffret *et al.*, Phys. Rev. Lett. **54**, 649 (1985).
[29]R. Cramer *et al.*, Z. Phys. C **29**, 513 (1985).
[30]V. M. Muzafarov, V. E. Troitskii, and S. V. Trubnikov, Sov. J. Part. Nucl. **14**, 467 (1983).
[31]M. Gourdin, Phys. Rep. C **11**, 30 (1974).
[32]E. L. Lomon, Ann. Phys. (N.Y.) **125**, 309 (1980).
[33]I. I. Belyantsev, V. K. Mitryushkin, P. K. Rashidov, and S. V. Trubnikov, J. Phys. G **9**, 871 (1983).
[34]L. Mathelitsch and H. F. K. Zingl, Nuovo Cimento A **44**, 81 (1978).
[35]M. Lacombe, B. Loiseau, R. Vinh Mau, J. Côté, P. Pirés, and R. de Tourreil, Phys. Lett. **101B**, 139 (1981).
[36]R. V. Reid, Ann. Phys. (N.Y.) **50**, 411 (1968).
[37]In a January 1989 experiment at Stanford Linear Accelerator Center (NE11), measurements of the neutron electric and magnetic form factors were made up to $Q^2=4$ (GeV/c)^2 using quasielastic electron-scattering (analysis in progress).
[38]R. G. Arnold, C. E. Carlson, and F. Gross, Phys. Rev. C **21**, 1426 (1980).
[39]M. J. Zuilhof and J. A. Tjon, Phys. Rev. C **24**, 736 (1981); **22**, 2369 (1980).
[40]R. S. Bhalero and S. A. Gurvitz, Phys. Rev. Lett. **47**, 1815 (1981); Phys. Rev. C **24**, 2773 (1981).
[41]T. Hamada and I. D. Johnston, Nucl. Phys. **34**, 382 (1962).
[42]P. L. Chung, F. Coester, B. D. Keister, and W. N. Polyzou, Phys. Rev. C **37**, 2000 (1988).
[43]R. Machleidt, K. Holinde, and Ch. Elster, Phys. Rep. **149**, 1 (1987).
[44]R. B. Wiringa, R. A. Smith, and T. L. Ainsworth, Phys. Rev. C **29**, 1207 (1984).
[45]I. L. Grach and L. A. Kondratyuk, Sov. J. Nucl. Phys. **39**, 198 (1984).
[46]L. L. Frankfurt and M. I. Strikman, Nucl. Phys. **B148**, 107 (1979); Phys. Rev. C **76**, 215 (1981).
[47]L. L. Frankfurt, I. L. Grach, L. A. Kondratyuk, and M. I. Strikman, Phys. Rep. Lett. **62**, 387 (1989).
[48]M. Gari and H. Hyuga, Nucl. Phys. **A264**, 409 (1976); M. Gari, H. Hyuga, and B. Sommer, Phys. Rev. C **14**, 2196 (1976).
[49]D. Berg *et al.*, Phys. Rev. Lett. **44**, 706 (1980).
[50]R. Dymarz and F. C. Khanna, Nucl. Phys. **A507**, 560 (1990).
[51]W. P. Sitarski, P. G. Blunden, and E. L. Lomon, Phys. Rev. C **36**, 2479 (1987); P. G. Blunden, W. R. Greenberg, and E. L. Loman, *ibid.* **40**, 1541 (1989).
[52]D. Allasia *et al.*, Phys. Lett. B **174**, 450 (1986).
[53]V. A. Matveev and P. Sorba, Lett. Nuovo Cimento **20**, 435 (1977).
[54]A. P. Kobushkin, Sov. J. Nucl. Phys. **28**, 252 (1978); A. P. Kobushkin and V. P. Sheelest, Sov. J. Part. Nucl. **14**, 483 (1983).
[55]Y. Yamauchi, M. Wakamatsu, and R. Yamamoto, Nucl. Phys. **A443**, 628 (1985).
[56]M. Chemtob and S. Furui, Nucl. Phys. **A454**, 548 (1986).
[57]P. Bosted and J. M. Laget, Nucl. Phys. **A296**, 413 (1978).
[58]H. Dijk and B. L. G. Bakker, Nucl. Phys. **A494**, 438 (1989).
[59]R. A. Arndt, J. S. Hyslop III, and L. D. Roper, Phys. Rev. D **35**, 128 (1987).
[60]T. S. Cheng and L. S. Kisslinger, Phys. Rev. C **35**, 1432 (1987).
[61]N. Honzawa, S. Ishida, Y. Kizukuri, M. Namiki, K. Okano, N. Oshimo, and M. Oda, Prog. Theor. Phys. **73**, 1502 (1985).
[62]T. H. R. Skyrme, Nucl. Phys. **31**, 556 (1962).
[63]E. Witten, Nucl. Phys. B **223**, 422 (1983).
[64]E. M. Nyman and D. O. Riska, Phys. Rev. Lett. **57**, 3007 (1986); Nucl. Phys. **A468**, 473 (1987).
[65]G. S. Adkins, C. R. Nappi, and E. Witten, Nucl. Phys. **B228**, 552 (1983).
[66]E. Braaten and L. Carson, Phys. Rev. D **39**, 838 (1989).
[67]S. J. Brodsky and B. T. Chertok, Phys. Rev. D **14**, 3003 (1976); S. J. Brodsky, C. R. Ji, and G. P. Lepage, Phys. Rev. Lett. **51**, 83 (1983); C. E. Carlson and F. Gross, Phys. Rev. D **36**, 2060 (1987).

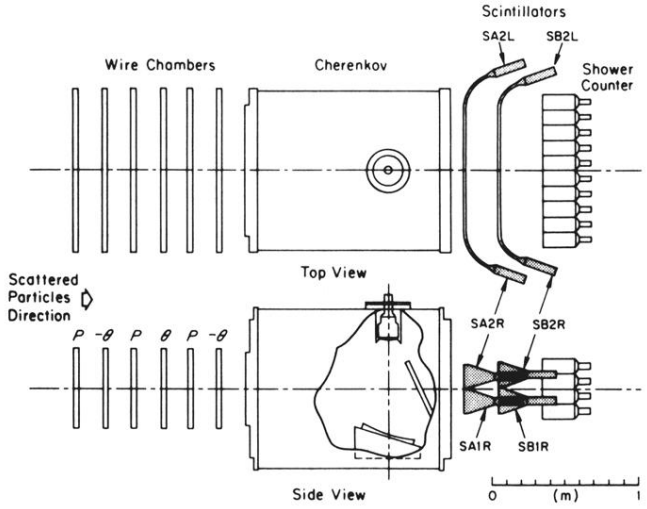

FIG. 7. The electron spectrometer detector arrangement. Particles entering from the left encountered six planes of wire chambers, a gas Čerenkov counter, two planes of scintillators, and a lead-glass shower counter.